

# Air Coils for Powering the Mu3e Experiment

von

**Moritz Hesping**



Bachelorarbeit in Physik  
vorgelegt dem Fachbereich Physik, Mathematik und Informatik (FB 08)  
der Johannes Gutenberg-Universität Mainz  
am 18. Juli 2019

1. Gutachter: Prof. Dr. Niklaus Berger
2. Gutachter: Jun.-Prof. Dr. Florian Hug

Ich versichere, dass ich die Arbeit selbstständig verfasst und keine anderen als die angegebenen Quellen und Hilfsmittel benutzt sowie Zitate kenntlich gemacht habe.

Mainz, den

Moritz Hesping  
AG Berger  
Institut für Kernphysik  
Staudingerweg 9  
Johannes Gutenberg-Universität D-55099 Mainz  
mhesping@students.uni-mainz.de

# Acknowledgments

I would like to thank Prof. Dr. Niklaus Berger for supervising my thesis and letting me be part of a big and exciting experiment like Mu3e. I would also like to thank Jun.-Prof. Florian Hug for being the second supervisor.

A big thank you also goes to my colleagues at AG Berger, whose friendliness made my time working with them a very pleasant one. I am especially grateful to Dr. Frederik Wauters, who introduced me to the subject matter and the equipment and was always available for questions.

I would like to thank Florian Gruber, my physics teacher in school. Without people like him getting students interested in the subject, very little research would get done in the world.

I am thankful to my friends and family who supported me while working on the thesis. Last but not least, I would like to thank everyone who proof read my thesis and provided me with valuable feedback.

# Abstract

The Mu3e experiment is searching for the charged lepton flavour violating decay of a positive muon into two positrons and an electron. Measuring such a decay would be a clear indication of new physics beyond the Standard Model. Mu3e is aiming for a sensitivity of two signal events in  $1 \times 10^{15}$  muon decays in the first phase of the experiment and ultimately one event in  $1 \times 10^{16}$  in the second phase. These sensitivities will be achieved using tracking and timing sensors inside a magnetic field.

One of the challenges in the design of Mu3e is designing the powering scheme. The power will be delivered to the detector interior at 20 V and stepped down to the operating voltages of the electronics by DC-DC buck converters there. These need to function inside of the experiment's 1 T magnetic field, which is why the inductors on the converters are replaced with air coils.

Due to their switching action, buck converters generate electromagnetic waves which can be conducted along the power supply or radiated by the air coils. These need to be suppressed, so that they do not disturb the sensors and electronics. Two methods to reduce the radiation are placing a shielding over the coils and using toroidal coils instead of solenoidal ones. In this thesis the viability of these methods was tested by designing prototypes and measuring the electromagnetic radiation as well as the efficiency of the converters. It was found that the shielding reduces the radiation by 5 dB and using toroidal coils reduces it by 30 dB, while only causing negligible losses in efficiency.

# Zusammenfassung

Das Mu3e Experiment sucht nach dem Zerfall eines positiven Myons in zwei Positronen und ein Elektron. Dieser Zerfall verletzt die Erhaltung des Flavours bei geladenen Leptonen. Einen solchen Zerfall nachzuweisen, wäre ein deutlicher Hinweis auf Physik jenseits des Standardmodells. Mu3e strebt eine Empfindlichkeit von zwei Signalen in  $1 \times 10^{15}$  Myonenzerfällen für die erste Phase des Experiments an und ein Signal in  $1 \times 10^{16}$  für die zweite Phase. Diese Empfindlichkeit wird durch Spur- und Timingsensoren in einem Magnetfeld erreicht.

Eine der Herausforderungen bei der Entwicklung von Mu3e ist das Design der Stromversorgung. Die Elektrizität wird bei 20 V ins Innere des Detektors geleitet, wo sie von Abwärtswandlern auf die Betriebsspannung der Elektronik gebracht wird. Diese müssen im 1 T starken Magnetfeld des Experiments funktionieren, weshalb die Induktoren der Wandler durch Luftspulen ersetzt werden.

Abwärtswandler erzeugen elektromagnetische Wellen, die durch die Stromversorgung geleitet und von den Spulen abgestrahlt werden können. Diese müssen unterdrückt werden, damit sie nicht die Sensoren und Elektronik stören. Zwei Methoden, um die Strahlung zu reduzieren, sind, eine Abschirmung über den Spulen zu platzieren und zylindrische Spulen durch torusförmige zu ersetzen. In dieser Arbeit wurde die Brauchbarkeit dieser Methoden getestet, indem Prototypen entwickelt und die elektromagnetische Strahlung der Abwärtswandler sowie ihre Effizienz gemessen wurden. Es wurde festgestellt, dass die Abschirmung die Strahlung um 5 dB reduziert und die Torusspule sie um 30 dB reduziert, wobei nur vernachlässigbar kleine Effizienzverluste verursacht werden.

# Contents

<b>1. Introduction</b>	<b>1</b>
<b>2. The Mu3e Experiment</b>	<b>3</b>
2.1. Charged Lepton Flavour Violating Decays . . . . .	3
2.2. Background . . . . .	4
2.3. Detector Geometry . . . . .	5
2.3.1. Pixel Sensors . . . . .	6
2.3.2. Timing Sensors . . . . .	6
2.4. Data Acquisition . . . . .	7
2.5. Power Requirements . . . . .	8
<b>3. Buck Converters and Air Coils</b>	<b>9</b>
3.1. Operating Principles of DC-DC Buck Converters . . . . .	9
3.2. Efficiency of Buck Converters . . . . .	11
3.3. Air Coils . . . . .	12
3.4. Electromagnetic Interference . . . . .	13
3.5. Reducing the Radiated Noise . . . . .	13
<b>4. Measurement Procedures</b>	<b>14</b>
4.1. Inductance . . . . .	14
4.1.1. With an Oscilloscope . . . . .	14
4.1.2. LCR Meter . . . . .	15
4.1.3. Inductance Measurement with Shielding . . . . .	15
4.2. Efficiency . . . . .	16
4.3. Radiated Noise . . . . .	17
4.3.1. Magnetic Near Field Probe . . . . .	18
4.3.2. Noise Measurement Rig . . . . .	19
4.3.3. Oscilloscope Settings . . . . .	20
4.4. Converter Chips Used in the Measurements . . . . .	20
<b>5. Part Design</b>	<b>22</b>
5.1. Shielding Boxes . . . . .	22
5.2. Toroidal Coil . . . . .	23
5.2.1. Plastic Core . . . . .	23
5.2.2. Optimization of Core Design Parameters . . . . .	24

*Contents*

<b>6. Results and Analysis</b>	<b>26</b>
6.1. Efficiency . . . . .	26
6.1.1. Effect of Shielding on the Inductance . . . . .	26
6.1.2. Effect of Shielding on the Efficiency . . . . .	26
6.1.3. Effect of Toroidal Coils on the Efficiency . . . . .	28
6.2. Radiated Noise . . . . .	29
6.2.1. Time Domain Signal . . . . .	29
6.2.2. Spectrum of the Frontend Converter . . . . .	30
6.2.3. Effect of Shielding on the Radiated Noise . . . . .	32
6.2.4. Effect of Toroidal Coils on the Radiated Noise . . . . .	35
6.2.5. Noise Radiated by the Wires . . . . .	36
<b>7. Conclusion and Outlook</b>	<b>38</b>
<b>Bibliography</b>	<b>40</b>
<b>A. Appendix</b>	<b>47</b>

# 1. Introduction

The Standard Model of particle physics was developed over the course of the second half of the last century. It is the theory describing all known fundamental particles, as well as three of the four fundamental interactions. It is one of the most successful scientific theories, with many of its predictions having been confirmed in experiments, the latest being the discovery of the Higgs boson at the Large Hadron Collider (LHC) in 2012, almost 50 years after its existence was predicted.

Successful as it is, there are phenomena the Standard Model cannot explain. The discovery of neutrino oscillations called for an extension of the Standard Model, taking into account finite masses of the neutrinos, which had been assumed massless by the Standard Model. The asymmetry between the amounts of matter and antimatter is too large to be explained by the few CP symmetry violating processes the Standard Model provides. Astronomical observations show the existence of dark matter, the mass of which explains, for example, the dynamics of galaxies, but which has not been observed to interact with known particles in any other way.

There are many theories trying to explain these phenomena. Finding experimental evidence for such physics beyond the Standard Model is the goal of many ongoing efforts in particle physics. There are two main ways of searching for new physics: Experiments at the energy frontier aim to collide particles at higher and higher energies, so that particles heavier than those known to the Standard Model might be directly produced in the collisions. Furthermore, the existence of particles predicted by new theories will slightly alter the likelihood of some processes. More precise measurement of the rates at which the processes happen let experiments at the intensity frontier indirectly discover particles many times more massive than what can currently be achieved at the energy frontier.

One experiment at the intensity frontier is the Mu3e experiment. It is looking to measure the decay of a muon into two positrons and an electron, which does not happen in the Standard Model. Discovering it would be an experimental proof for theories beyond the Standard Model. If it is not discovered, the upper limit for its existence is a constrain for such theories.

The goal of Mu3e is to reach a sensitivity of one event in  $1 \times 10^{16}$  muon decays. This requires a large design effort to reach the necessary vertex, timing and momentum resolution. A part of this is the design of the powering scheme for the detectors and readout electronics. The power needs to be supplied at a higher voltage for efficient

## *1. Introduction*

transport, which is then stepped down near the devices to their operating voltage. The momentum measurements in Mu3e happen by deflecting the electrons and positrons in a strong magnetic field and reconstructing the momenta from the curve of the trajectories. This means that the DC-DC buck converters used for stepping down the voltage need to function inside the magnetic field. They are adapted for this by replacing their standard ferrite core inductors with air coils.

The current through these coils is oscillating as part of the operation of the converters. This way they produce electromagnetic waves, which could potentially disturb the functioning of other electronics in the experiment. In this thesis two methods of reducing this radiation were tested. Prototypes of copper boxes for shielding and of a toroidal coil were designed. They were then tested with the converters and the radiation and efficiency were measured to assess the viability of these methods.

## 2. The Mu3e Experiment

### 2.1. Charged Lepton Flavour Violating Decays

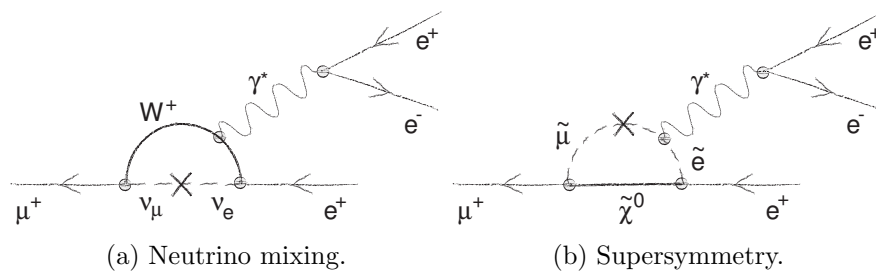


Figure 2.1.: Feynman graphs for possible channels for the  $\mu \rightarrow eee$  decay.

In the Standard Model of particle physics there are three flavours of charged leptons [1]: The electron, the muon and the tau. To each of these belongs a corresponding neutrino, which is electrically neutral and, in the Standard Model, without mass. In addition there are the antiparticles of the charged and uncharged leptons. In the Standard Model lepton flavour is conserved. This means that in a reaction, the lepton family number  $N_l$  is conserved [2]:

$$N_l = N(l) - N(\bar{l}) + N(\nu_l) - N(\bar{\nu}_l) = \text{const.} \quad (2.1)$$

where  $l$  is one of the lepton families. For example, the reaction  $n \rightarrow p + e^-$  is forbidden, because the initial state has  $N_e = 0$  and the final state has  $N_e' = 1$ . The beta decay  $n \rightarrow p + e^- + \bar{\nu}_e$  on the other hand conserves lepton flavour.

Contrary to the standard model assumption, neutrinos have a very small but finite mass. Over time this causes them to change from one flavour to another. This effect is called neutrino oscillations and has been observed for neutrinos from the sun, nuclear reactors, the upper atmosphere and accelerators.

To date no flavour violation has been observed with charged leptons. One such process could be the decay of an anti muon into two positrons and an electron:

$$\mu^+ \rightarrow e^+ + e^+ + e^-. \quad (2.2)$$

This process is theoretically possible through neutrino mixing, however with a branching fraction below  $10^{-54}$  it cannot be observed. Several proposed extensions

## 2. The Mu3e Experiment

to the Standard Model predict a higher branching fraction for the  $\mu \rightarrow eee$  decay. Any such model is therefore constrained by the experimental upper limit of this branching fraction and an observation of this decay would be a sign for physics beyond the Standard Model. In Fig. 2.1 Feynman graphs for the decay with neutrino mixing and supersymmetry, one possible extension to the Standard Model, are shown.

The most sensitive search for  $\mu \rightarrow eee$  so far was done by the SINDRUM experiment, where the upper limit for the branching fraction could be set to  $1.0 \times 10^{-12}$ . The Mu3e experiment aims to improve on this with a sensitivity of one signal event in  $1 \times 10^{16}$  muon decays [3].

### 2.2. Background

There are two main contributions to the background in the Mu3e experiment. One is the internal conversion process

$$\mu^+ \rightarrow e^+ + e^+ + e^- + \nu_\mu + \bar{\nu}_e. \quad (2.3)$$

Since the neutrinos are invisible to the detector, this background can only be distinguished by the energy and momentum they carry away. The Feynman graph of the internal conversion process is shown in Fig. 2.2. The other main contribution to the background are accidental combinations of two positrons and an electron. For example, a positron might originate from a Michel decay

$$\mu^+ \rightarrow e^+ \bar{\nu}_e \nu_\mu, \quad (2.4)$$

which is the most common decay channel of the muon and an electron positron pair from Bhabha scattering or pair production. If they originate close to each other, they might be mistaken for a  $\mu \rightarrow eee$  event. The signal and this combinatorial background are illustrated in Fig. 2.3. To distinguish the signal from this background, good timing, vertex and momentum resolution is needed. To achieve the sensitivity of one signal in  $10^{16}$  muon decays Mu3e is aiming for, the timing resolution needs to be about 100 ps, the momentum resolution about 300 keV/c and the vertex resolution about 200  $\mu\text{m}$  [4].

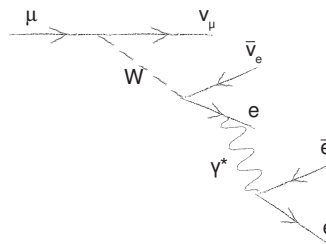


Figure 2.2.: Feynman graph of the internal conversion process.

## 2. The Mu3e Experiment

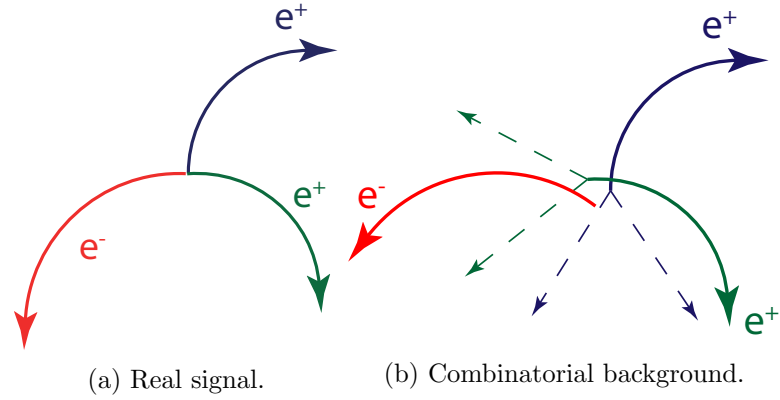


Figure 2.3.: Topology of a  $\mu \rightarrow eee$  event and an example of combinatorial background.

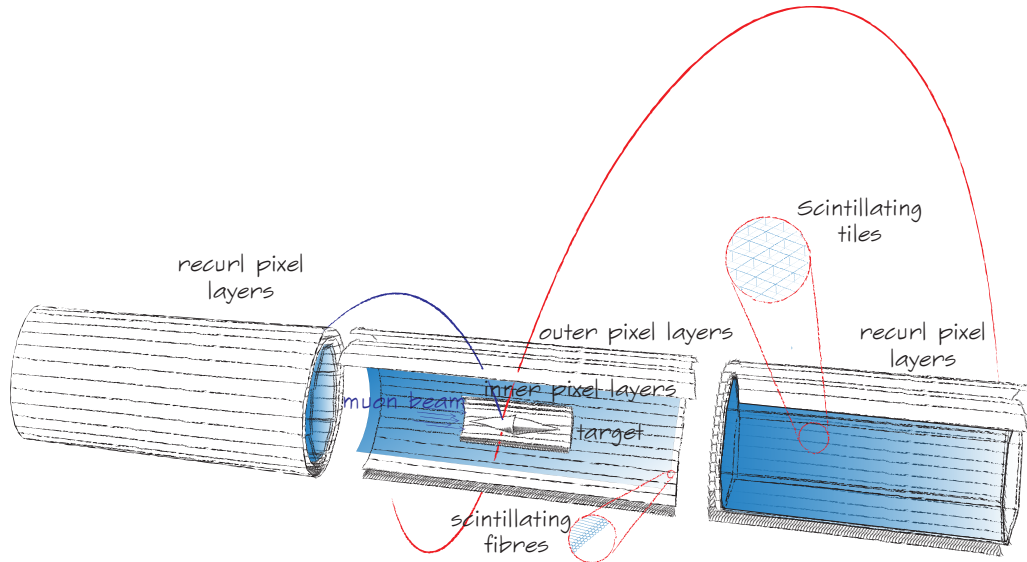


Figure 2.4.: Schematic of the different detectors in the Mu3e experiment. An example of tracks from a  $\mu \rightarrow eee$  event is shown, with the positrons in red and the electron in blue.

### 2.3. Detector Geometry

The Mu3e experiment will take place at the Paul Scherrer Institute (PSI) in Switzerland, where the accelerator with the world's most intense proton beam is located. It produces up to 2.4 mA of 590 MeV/c protons. In collisions with graphite targets, pions are produced, which then decay to muons. This way, the  $\pi^+e^-$  beamline at PSI provides up to  $10^8$  positive muons/s with momenta around 29 MeV/c. A muon beam line with up to  $10^{10}$  muons/s is currently under study at PSI, which is required for the

## 2. The Mu3e Experiment

target sensitivity of Mu3e. The muons are stopped in a target in the shape of a hollow double cone, where they decay. The experiment is placed inside of a 1 T solenoidal magnetic field. This causes the tracks of the electrons and positrons produced in the decays to curve. From the curvature their momenta can be inferred. The geometry of the experiment with the different detectors used is illustrated in Fig. 2.4.

### 2.3.1. Pixel Sensors

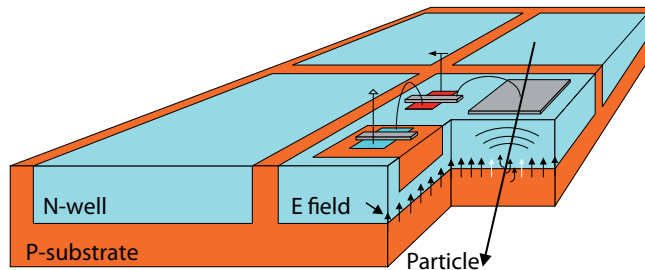


Figure 2.5.: Sketch of a high voltage monolithic active pixel sensor (from [5]).

As tracking sensors, High Voltage Active Monolithic Pixel Sensors (HV-MAPS) are used. These not only possess the necessary spatial resolution but can be thinned to  $50\ \mu\text{m}$  [6]. This is important, since for the relatively low momenta of the electrons and positrons multiple Coulomb scattering has a large influence on the precision of the momentum measurements, which necessitates a low material budget.

The pixels of the HV-MAPS are n-wells in a p-doped substrate as shown in Fig. 2.5. A bias voltage of about 80 V is applied across these. When ionizing radiation passes through a pixel, charges in the semiconductor are released and collected via drift. The high voltage used in these sensors gives them a faster charge collection than regular monolithic active pixel sensors.

For Mu3e a series of custom HV-MAPS is being developed, called MuPix. As shown in Fig. 2.4, there are three sets of pixel detectors. Two layers are close to the target to precisely measure the origin of the particles' tracks. Two layers at a larger radius serve the momentum measurement. Both before and after the target are pixel layers that detect the recurling particles. The momentum resolution from these recurling tracks is up to ten times better than where only the outgoing part of the track is detected [3].

### 2.3.2. Timing Sensors

In the Mu3e experiment scintillators in combination with silicon photomultipliers are used for precise timing. Near the target, where material budget is a concern, three layers of scintillating fibres with a diameter of  $250\ \mu\text{m}$  are used. After the recurl pixel

## 2. The Mu3e Experiment

layers the tracks are no longer needed and 0.5 cm thick scintillating tiles offer a more precise timing measurement. In prototypes time resolutions of 572 ps for the fibres and 70 ps for the tiles were achieved. The signal from the photomultipliers is read out and digitized by custom Application Specific Integrated Circuit (ASIC) called MuTRiG [7].

### 2.4. Data Acquisition

At the targeted rate of  $2 \times 10^9$  muons/s the sensors in the experiment will generate about  $1 \text{ Tbit s}^{-1}$  of data [4]. It is necessary to reduce this to less than  $100 \text{ MB s}^{-1}$  before it can be written to disk. For each type of detector the data is sorted in time by the frontend Field Programmable Gate Arrays (FPGA) and sent to the switching board FPGAs over optical links. These combine the data from all detectors into 50 ns time slices. More FPGAs distribute the time slices among PCs with powerful Graphics Processing Units (GPU). Each PC receives the data of the entire experiment for a time slice, as this is required for reconstructing the recurling tracks. On the GPU, the tracks of the particles are reconstructed and classified as electrons and positrons. Then events are selected, in which three tracks originate from the same point [8].

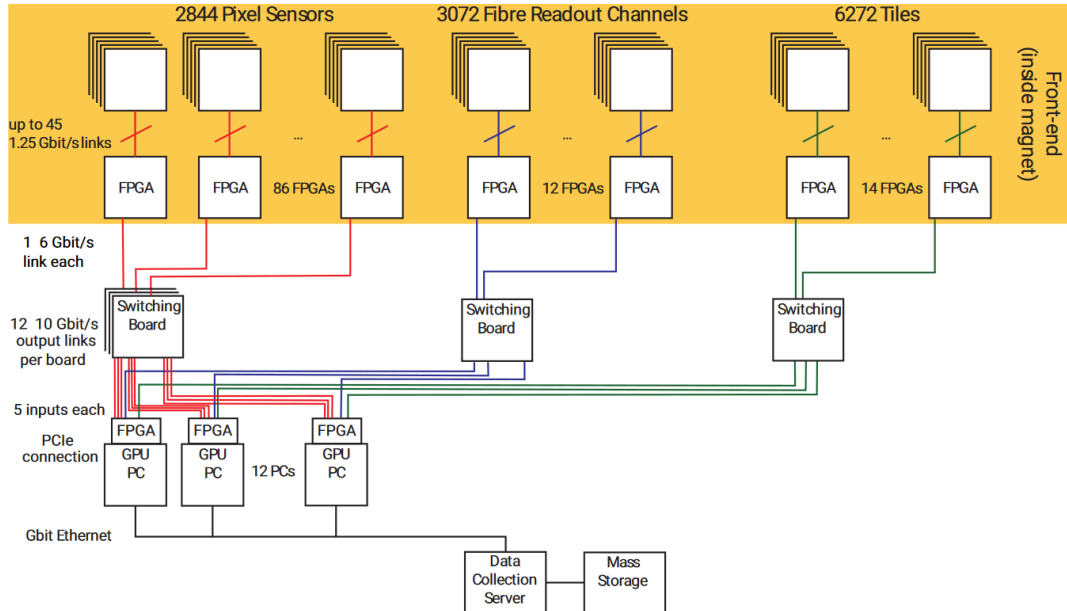


Figure 2.6.: Readout scheme of the Mu3e experiment. The yellow area indicates the electronics which are inside of the magnet (from [8]).

## 2.5. Power Requirements

The electronics in the experiment need to be supplied with power. The power of direct current (DC) is  $P = IV$  with the current  $I$  and the voltage  $V$ . In a conductor with resistance  $R$  there are ohmic losses  $P_{\text{loss}} = RI^2$ . To reduce losses in the cables the power therefore needs to be transported at a higher voltage of 20 V and then stepped down to the operating voltages of the electronics. This is especially important in Mu3e, as spatial restrictions and the need for a low material budget limit the thickness of the power cables. The voltage will be controlled using DC-DC buck converters, which are discussed in section 3.1. There are three main types of components requiring buck converters: The MuPix sensors, the MuTRiG chip and the frontend boards.

The sensors are divided into partitions, to each of which belongs a frontend board. The frontend boards contain all electronics necessary for sorting the electrical signal from the detectors in time and converting them into optical signals. This includes the frontend FPGAs. Each frontend board features three buck converters with different voltages to accommodate its different components. The requirements for the different components are listed in Table 2.1. The voltages for MuPix and MuTRiG include the voltage drop over the connection from the converter to the chip and in the low drop out regulators on the chips.

Component	Quantity	Voltage [V]	Typical current [A]	Maximum current [A]	Power [W]	Total [W]
MuPix partition	86	2.3	20	30	46	3965
MuTRiG partition	26	2.3	10	30	23	598
Frontend board	112	1.1	2	3	2.2	246.4
	112	1.8	1	1.5	1.8	201.6
	112	3.3	2.5	3.5	8.25	924

Table 2.1.: Voltage and power requirements for ASICs and on-detector electronic components inside of the magnet.

## 3. Buck Converters and Air Coils

### 3.1. Operating Principles of DC-DC Buck Converters

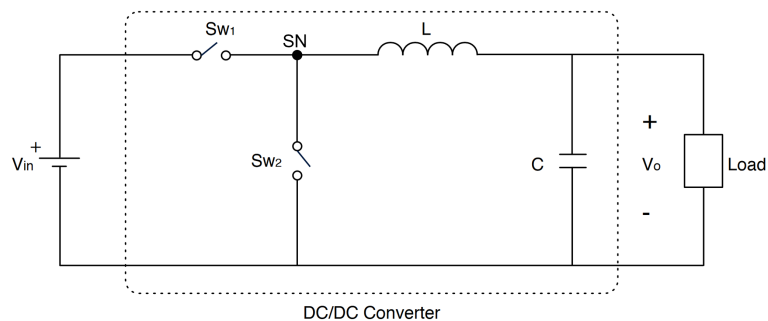


Figure 3.1.: Schematic of a simple DC-DC buck converter (adapted from [9]).

A DC-DC Buck converter provides a constant output voltage  $V_o$  that is lower than the input voltage  $V_{in}$ . Its main components are two transistors acting as switches, an inductor and a capacitor. The schematic of a simple converter is shown in Fig. 3.1, not featured are the electronics controlling the switches. The two switches are opened and closed alternately. From time  $t = 0$  to  $t = t_{on}$  switch 1 is closed and switch 2 is open and from  $t = t_{on}$  to  $t = t_{on} + t_{off} = T$  switch 1 is open and switch 2 is closed. The voltage at the switching node ("SN" in Fig. 3.1) is plotted over one period  $T$  in Fig. 3.2. During the operation of the converter the switching frequency  $f_s = 1/T$  is constant, while the duty cycle  $D = t_{on}/T$  is modulated to control the output voltage. As illustrated in Fig. 3.3, the buck converter can be simplified as a smaller circuit at

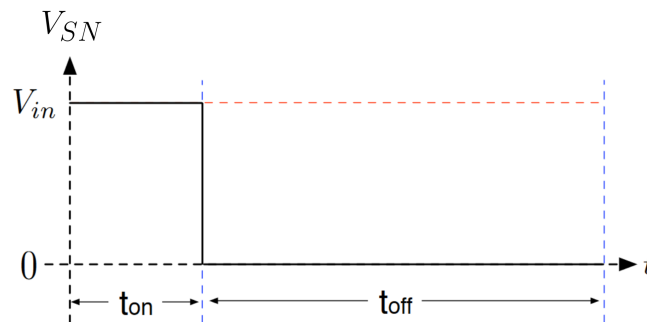


Figure 3.2.: The voltage at the switching node (adapted from [9]).

### 3. Buck Converters and Air Coils

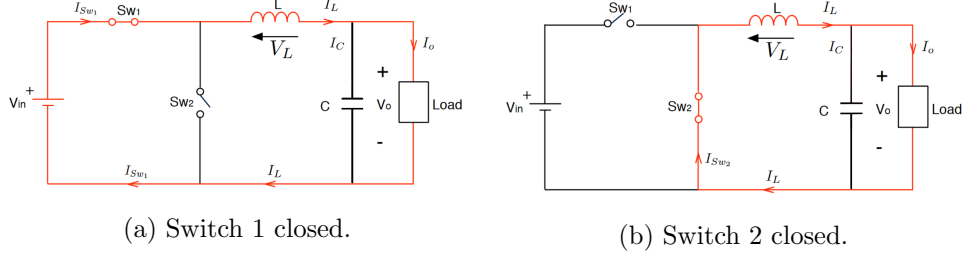


Figure 3.3.: The two stages of the operation of a buck converter. The red lines indicate the current (from [9]).

the different phases of its operation. While switch 1 is closed, the voltage drop  $V_L$  across the inductor can be calculated according to Kirchoff's second rule as

$$V_L(0 \leq t \leq t_{on}) = V_{in} - V_o \quad (3.1)$$

and while switch 2 is closed it is

$$V_L(t_{on} \leq t \leq T) = -V_o. \quad (3.2)$$

The second switch can also be replaced with a diode, which prevents a short when switch 1 is closed but lets the current flow the same way switch 2 would when switch 1 is open. The current flowing through an inductor is related to the voltage across it by

$$V_L(t) = -L \frac{dI_L(t)}{dt}. \quad (3.3)$$

Integrating over  $t$  gives the current over time

$$I_L(t) = \begin{cases} \frac{V_{in}-V_o}{L}t + I_L(0) & 0 \leq t \leq t_{on} \\ \frac{-V_o}{L}t + I_L(t_{on}) + \frac{V_o}{L}t_{on} & t_{on} \leq t \leq T \end{cases}. \quad (3.4)$$

Plots of the voltage and current of the inductor are shown in Fig. 3.4. The peak to peak difference in current is

$$I_{PP} = I_L(t_{on}) - I_L(0) = \frac{V_{in} - V_o}{L}t_{on}. \quad (3.5)$$

Since the operation of the buck converter is periodical, so should be the current:  $I_L(0) = I_L(T)$ . Substituting Equation 3.4 and solving for  $V_o$  yields

$$I_L(0) = \frac{-V_o}{L}T + \frac{V_{in} - V_o}{L}t_{on} + I_L(0) + \frac{V_o}{L}t_{on} \quad (3.6)$$

$$V_o = DV_{in}. \quad (3.7)$$

This shows that the output voltage can be regulated by controlling the duty cycle. The capacitor in parallel to the load charges and discharges over the cycle, which smooths out the output voltage.

### 3. Buck Converters and Air Coils

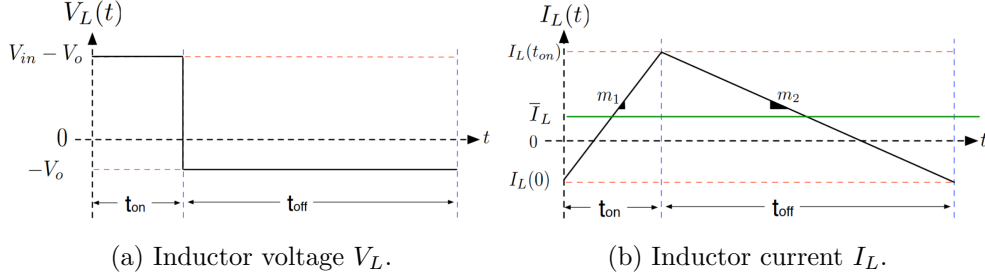


Figure 3.4.: Inductor voltage and current over time (from [9]).

## 3.2. Efficiency of Buck Converters

The efficiency of a buck converter is defined as

$$\eta = \frac{P_o}{P_{in}}, \quad (3.8)$$

where  $P_o = V_o I_o$  is the output power and  $P_{in} = V_{in} I_{in}$  is the input power. Several effects contribute to losses in the converter, however in the scope of this thesis only those related to the inductor will be discussed, which are ohmic losses in the transistors and in the coil [10]. The losses in the transistors are given by

$$P_{sw1} = \left( I_o^2 + \frac{I_{PP}^2}{12} \right) \cdot R_{on,sw1} \cdot \frac{V_o}{V_{in}} \quad (3.9)$$

$$P_{sw2} = \left( I_o^2 + \frac{I_{PP}^2}{12} \right) \cdot R_{on,sw2} \cdot \left( 1 - \frac{V_o}{V_{in}} \right) \quad (3.10)$$

where  $R_{on,sw1}$  and  $R_{on,sw2}$  are the on-resistances of switch 1 and switch 2 respectively. The conductive loss in the inductor is given by

$$P_L = \left( I_o^2 + \frac{I_{PP}^2}{12} \right) \cdot R_{DC} \quad (3.11)$$

where  $R_{DC}$  is the direct current resistance of the inductor. The peak to peak difference in current  $I_{PP}$  is given by Equation 3.5, which can be rewritten as

$$I_{PP} = \frac{V_{in} - V_o}{f_s L} \cdot \frac{V_o}{V_{in}}. \quad (3.12)$$

According to these equations a higher inductance will lead to a more efficient converter. In practice, however, increasing the inductance of the inductor will likely also increase its DC resistance, which will counteract the improvement to some extent. An example of a buck converter efficiency curve in relation to output current is shown in Fig. 3.5. In the figure there are different curves for Discontinuous Conduction Mode (DCM), in which the output current is zero for part of the cycle, and Forced Continuous Conduction Mode (FCCM), where there always is an output current. In the measurement the converters were always operated in FCCM.

### 3. Buck Converters and Air Coils

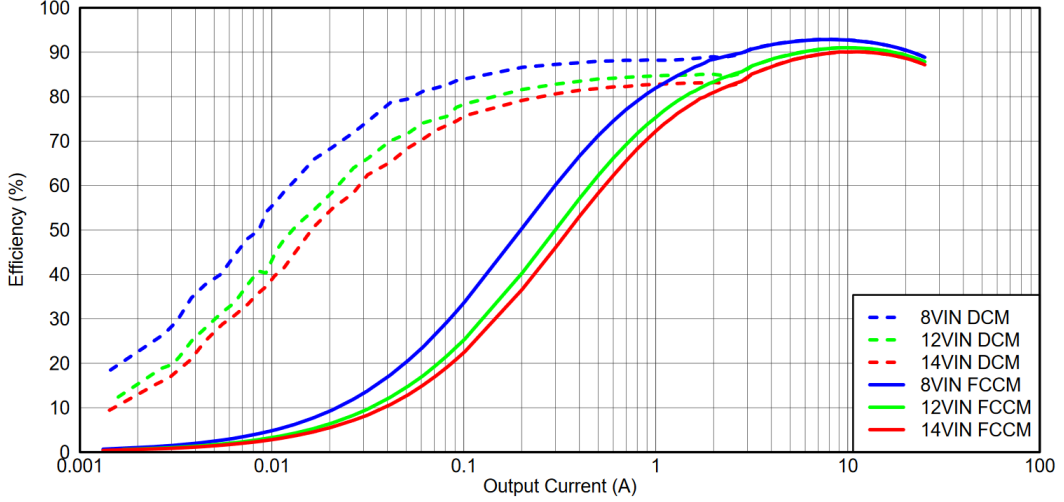


Figure 3.5.: Efficiency curve of the TPS53819A buck converter (from [11]).

### 3.3. Air Coils

Commercial buck converters use inductors with a ferrite core. These can be much more compact than an air coil, which do not have such a core to amplify their magnetic field. However, they cannot be used in the Mu3e experiment. The buck converters need to be placed close to the electronics they are powering, which is inside the 1 T magnetic field. This would saturate the inductor cores and thus inhibit the functioning of the converters. The inductors therefore need to be replaced with air coils, which do not suffer from this effect. The two common types of coil used in this thesis are solenoidal and toroidal coils. The inductance  $L$  of a solenoidal coil is given by

$$L = \mu_0 K N^2 \frac{A}{l}, \quad (3.13)$$

where  $\mu_0 = 4\pi 10^{-7} \text{ H m}^{-1}$  is the permeability of free space,  $K \approx 1$  is the Nagaoka coefficient, which is a correction factor for the finite length of the coil [12],  $N$  is the number of windings,  $A$  is the cross-sectional area of the coil and  $l$  is the length of the coil.

The inductance of a toroidal coil with a rectangular cross-section is approximately [13]

$$L = \frac{\mu_0}{2\pi} N^2 H \ln \left( \frac{r_o}{r_i} \right), \quad (3.14)$$

where  $H$  is the height of the toroid,  $r_o$  is the outer radius and  $r_i$  is the inner radius as shown in Fig. 3.6. The toroid has the advantage that its magnetic field is more contained than the one of the solenoid, this however comes at the cost of a larger physical size and a longer length of wire, which increases the DC resistance of the coil.

### 3. Buck Converters and Air Coils

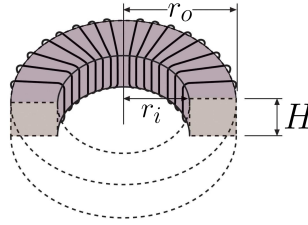


Figure 3.6.: A toroidal coil with rectangular cross section (adapted from [14]).

## 3.4. Electromagnetic Interference

An electronic circuit may be disturbed in its function when exposed to signals from the outside. Such signals might reach it by conduction through its in- and output wires or through changing electromagnetic fields. In a buck converter, the voltage and current oscillate as shown in Fig. 3.4. This causes the magnetic field of the coil to also change in time, which causes electromagnetic waves to radiate away from the coil. Similarly, oscillations in voltage and current can be transmitted through the wires both towards the power supply and the load. It is important to counteract these effects so they do not impede the proper functioning of other equipment in the experiment. In the following the electromagnetic interference will simply be referred to as conducted or radiated noise respectively.

## 3.5. Reducing the Radiated Noise

Two methods for reducing the noise radiated by the converters are shielding and solenoidal coils. A shielding placed over the coil will attenuate the electromagnetic waves to some degree. The field of a toroidal coil is more contained than that of a solenoid, so the toroid will radiate less. However, both of these methods come at a cost. The shielding will slightly lower the inductance of the coil and the toroid has a higher DC resistance than a solenoid of comparable inductance. Both these effects will decrease the efficiency of the converter, as discussed in section 3.2. It is therefore necessary to investigate, whether the improvement in noise reduction outweighs the potential drawbacks. This was studied in this thesis by creating prototypes of both shielding and a solenoidal coil and making comparative measurements of the efficiency and radiated noise of the boards with and without these methods applied.

## 4. Measurement Procedures

### 4.1. Inductance

#### 4.1.1. With an Oscilloscope

There are several methods for measuring inductances using a function generator and an oscilloscope. The first one [15] involves constructing a low pass filter from the inductor and a known resistor  $R_{ref}$ . The circuit is driven by a sine wave generator and the output signal is viewed on the oscilloscope. The frequency is then adjusted until the output amplitude is half of the output amplitude with the inductor removed. The inductance is then

$$L = \sqrt{\frac{1}{3} \frac{R_{ref}}{2\pi f_{\frac{1}{2}}}}, \quad (4.1)$$

where  $f_{\frac{1}{2}}$  is the frequency at which the output amplitude is halved.

Secondly a tank circuit can be built from the inductor and a known capacitor  $C_{ref}$ . It is driven with a sine wave and the output is observed on the oscilloscope. The frequency is adjusted to find the resonant frequency from which the inductance can be determined as

$$L = \frac{1}{(2\pi f_0)^2 C_{ref}}, \quad (4.2)$$

where  $f_0$  is the resonant frequency.

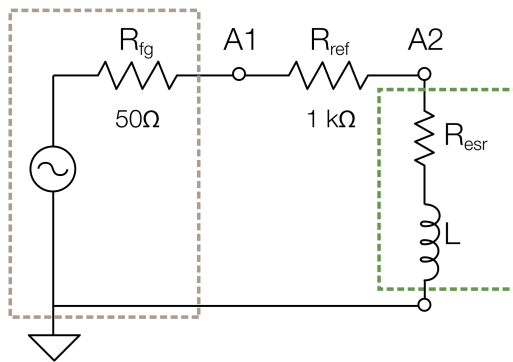


Figure 4.1.: Setup for measuring an inductor (green box) via the impedance (from [16]).

#### 4. Measurement Procedures

Lastly the inductor and a known resistor  $R_{ref}$  can be combined as shown in Fig. 4.1. A sine wave of frequency  $f$  is applied and the voltages at the points A1 and A2 are viewed on the scope. The amplitudes  $V_{A1}$  and  $V_{A2}$  and the phase difference  $\theta$  are measured. From these the magnitude  $Z$  and phase  $\alpha$  of the inductor's impedance are calculated and from those the inductance and equivalent series resistance  $R_{esr}$ :

$$Z = \frac{V_{A1}f}{\sqrt{V_{A1}^2 - 2V_{A1}V_{A2}\cos(\theta) + V_{A2}^2}} \quad (4.3)$$

$$\alpha = \theta - \arctan\left(\frac{-V_{A2}\sin(\theta)}{V_{A1} - V_{A2}\cos(\theta)}\right) \quad (4.4)$$

$$R_{esr} = Z \cos \alpha \quad (4.5)$$

$$L = \frac{Z \sin \alpha}{2\pi f} \quad (4.6)$$

All of these methods were attempted, but no setup with a good precision and consistency was achieved. For this reason a commercial LCR meter was bought and used for the inductance measurements.

##### 4.1.2. LCR Meter

LCR meters are instruments that can measure an electronic component's inductance, resistance and capacitance. The functioning principle behind this is similar to the last method described in subsection 4.1.1: The meter drives the component with a sinusoidal voltage and measures the amplitude and relative phase of the resulting current. From those the impedance is calculated. Assuming that the component can be modelled as pure inductance, resistance and capacitance either in series or in parallel, these can then be calculated from the impedance. Crucially, this means that the value the LCR meter indicates depends on the frequency and the mode (serial or parallel) the meter is set to. The meter used is a BK Precision 880. It can be set to 100 Hz, 120 Hz, 1 kHz, 10 kHz and 100 kHz. An inductance measurement is shown as an example in Fig. 4.2. In all measurements in the following the frequency was set to 100 kHz, as this is closest to the 1 MHz switching frequencies of the buck converters that were tested and also the accuracy of the meter is best at this setting. The meter was set to parallel mode, as per the recommendation of the user manual [17].

##### 4.1.3. Inductance Measurement with Shielding

To determine the effect of shielding on the inductance of a coil, it was measured with the different copper boxes described in section 5.1. When the converter is operated with these boxes, the circuit board itself closes off the open side of the box. However, it is not possible to measure the inductance of the coil while it is soldered to the board. To keep the measurement as close to the real situation as possible, the coil was unsoldered from the TPS548A20 evaluation module, but placed in its spot for the measurement.

#### 4. Measurement Procedures

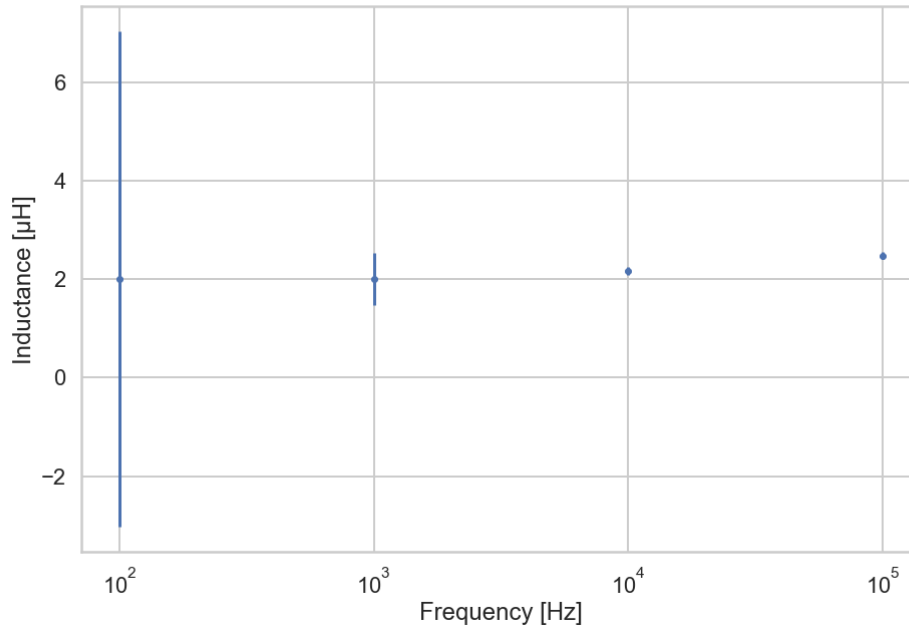


Figure 4.2.: Example measurement of an inductor at the different frequencies of the LCR meter.

### 4.2. Efficiency

To measure the efficiency of a buck converter, according to Equation 3.8 the input and output currents and voltages need to be measured. The input power was delivered by a Tenma 72-2635 programmable power supply [18]. The voltage and current of this supply can be set and read out by a serial data interface. It was set to supply a constant voltage. If the input current exceeds the current limit set at the supply, the voltage is lowered accordingly. The converter was connected to a Statron Typ 3229 load generator, which draws a constant load current from a device under test. The load current can also be controlled and read remotely. While the load generator also displays the voltage, this was not used for the measurements. Due to the high currents involved, there was a significant voltage drop in the connecting wires. For this reason, the output voltage was measured directly at the output connectors of the converter using a multimeter. A python script was used to ramp the load current and record the input voltage, input current and output voltage for each step. A photograph of the setup is shown in Fig. 4.3.

## 4. Measurement Procedures

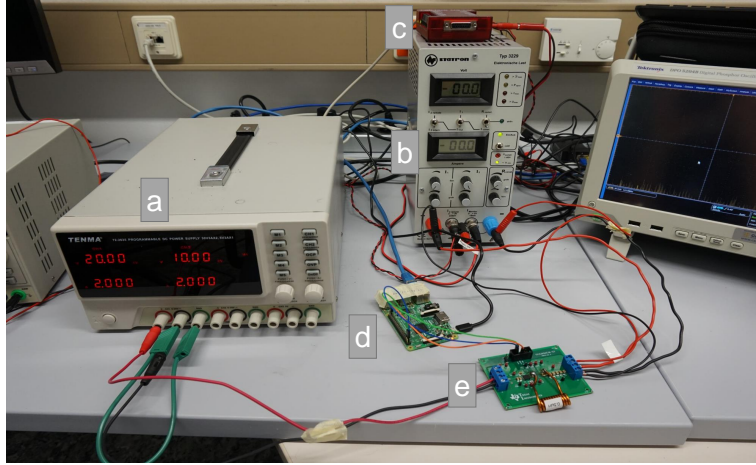


Figure 4.3.: Efficiency measurement setup. a) power supply b) load generator c) Lab-Jack connecting load generator to computer d) Raspberry Pi e) MuPix converter.

### 4.3. Radiated Noise

To measure the electromagnetic noise radiated by the buck converter coils, the converter was attached to the load the same way as in section 4.2, though at a constant load current. The magnetic field of the coil was then measured using a magnetic near field probe and an oscilloscope. The different parts of this setup, which is shown in Fig. 4.4, are described in more detail in the following sections.

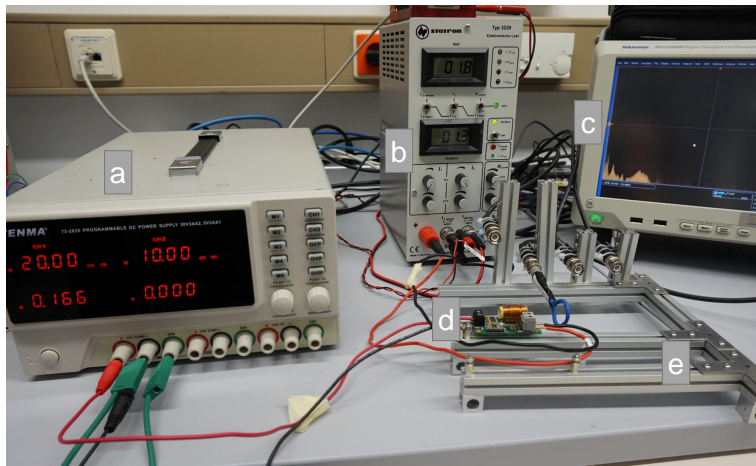


Figure 4.4.: The noise measurement setup. a) power supply b) load generator c) oscilloscope d) front end converter e) noise measurement rig with probe.

## 4. Measurement Procedures

### 4.3.1. Magnetic Near Field Probe

Near field probes are used to identify conducted and radiated noise in electronic circuits. There are two types: E-field probes measure electric fields and H-field probes measure magnetic fields. To measure the noise radiated by the coils on the buck converters an H-field probe was used.

The simplest design of such a probe is a loop of wire. A changing magnetic field induces a voltage in the loop, which can be picked up by an oscilloscope or spectrum analyzer. For the noise measurements a more sophisticated design [19] was used, which includes shielding from electric fields. The schematic for such a probe is shown in Fig. 4.5. As the inner conductor a copper wire of 1.5 mm diameter was used. This was isolated from the outer conductor by a layer of heat shrink tubing. The shielding was made by wrapping copper tape around this, leaving a gap in the middle. One end of the wire was inserted in the central contact of a BNC connector. The other end of the wire and the shielding were soldered to the outside of the connector. The finished probe is shown in Fig. 4.6.

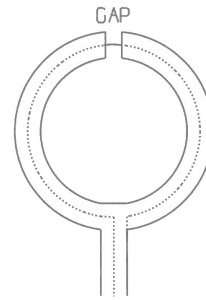


Figure 4.5.: Schematic of the magnetic near field probe (adapted from [19]).

The power output of magnetic field probes is dependent on the frequency of the radiated noise it is measuring. This is due to the inductance and capacitance of the probe. The power rises with frequency at first until it approaches the resonance frequency of the probe, where it dips down. Larger probes have a lower resonance frequency. Figure 4.7 shows an example of such power curves. The probe has a diameter of about 25 mm. By comparing this to commercial probes [20], its resonance frequency can be estimated to be around 500 MHz.



Figure 4.6.: The magnetic near field probe used for the noise measurements.

#### 4. Measurement Procedures

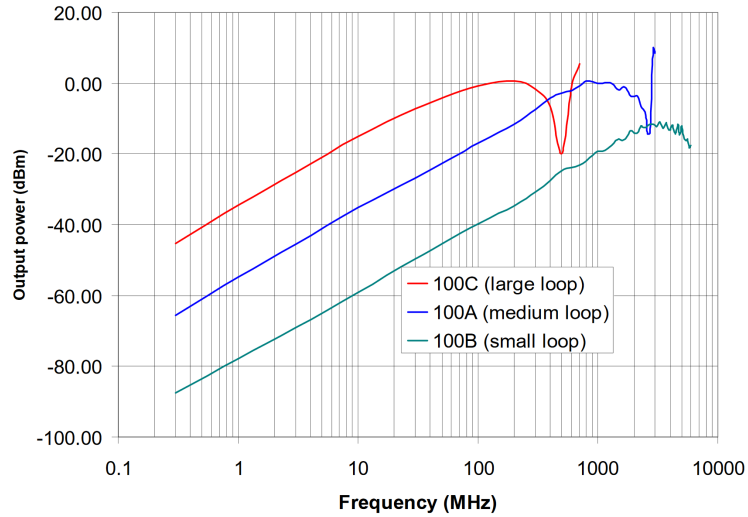


Figure 4.7.: Output power at 1 mT of different loop probes against frequency (from [20]).

#### 4.3.2. Noise Measurement Rig

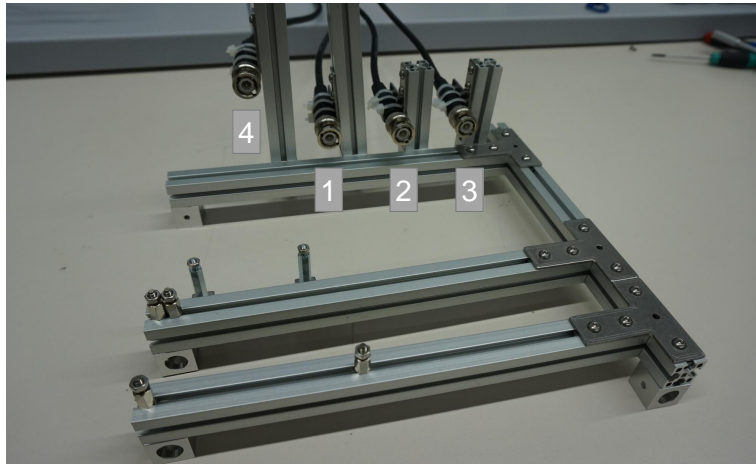


Figure 4.8.: The noise measurement rig with the four probe positions.

The strength of the magnetic field of a coil strongly depends on the distance to the coil. It is therefore important to keep the position of the probe as consistent as possible, if a comparison between the amplitudes of two measurements is to be made. For this purpose, a rig was constructed using the MakerBeam system. It is shown in Fig. 4.8.

## 4. Measurement Procedures

The buck converter under test is screwed to the rig. At several points BNC cables are attached to the rig, three along the axis of a solenoidal coil and one above the board. The probe can be plugged into these cables and is this way at a set distance from the board. Four identical cables were used to minimize any effect their impedance might have on the measurement.

This setup does not control the orientation of the probe, which can rotate along its long axis. Since the magnetic flux through the loop and with it the signal strength depend on the probe's orientation, the probe had to be carefully adjusted to the same orientation for each measurement. The noise was measured in two orientations: With the probe vertical like the windings of the solenoid coils and with the probe horizontal. The sign of the voltage induced in the probe depends on the orientation, turning the probe by  $180^\circ$  will flip it. The orientation of the probe was chosen to make the sign match the one of the voltage across the coil (see also subsection 6.2.1). The orientation was marked with a label on the probe for consistency, as can be seen in Fig. 4.6.

### 4.3.3. Oscilloscope Settings

The oscilloscope used for the measurements is a Tektronix DPO 5204B [21]. The input impedance of the oscilloscope was set to  $50\ \Omega$  to avoid reflections of the signal. Most measurements were done in the frequency domain. For this the oscilloscopes built-in Fast Fourier Transform (FFT) function was used. The sampling rate of the oscilloscope was set to  $2.5 \times 10^9$  Samples/s. The frequency range of the FFT was automatically set to the corresponding Nyquist frequency of 1250 MHz. This is much higher than the switching frequency  $f_s = 1$  MHz of the converters and should therefore be sufficient to see all interesting structures of the spectra. The time scale was set to  $100\ \mu\text{s}/\text{div}$ . This results in a record length of  $1.6 \times 10^6$  sample points. A higher record length results in a better frequency resolution, thus the highest value at which the oscilloscope remained reasonably responsive was chosen. The vertical scale of the time domain signal was chosen as fine as possible while keeping it on the screen entirely. This turned out to be  $7\ \text{mV}/\text{div}$ . The complete list of parameters for the noise measurements can be found in Table A.1.

## 4.4. Converter Chips Used in the Measurements

The buck converters used in Mu3e are based on commercial DC-DC buck converters by Texas Instruments, which are modified with custom air coils. The converters for the frontend boards use the TPS548A20 chip which includes both the controller and switches of the converter. The evaluation module for this chip, with the inductor replaced for an air coil, was used for initial tests of the measurement methods. For the final measurements with the shielding boxes the second version of a prototype board incorporating this chip was used, which was developed for Mu3e in Mainz and Heidelberg. This converter is here in referred to as "frontend converter". The converters for the MuPix and MuTRiG chips use the TPS53819A controller and the

#### 4. Measurement Procedures

CSD87350Q5D switch. A first prototype using these chips is currently being tested. For the measurements for the comparison between solenoid and toroid the evaluation board with these chips [11] were used. It is here referred to as "MuPix converter". The switching frequency of this evaluation module is 425 kHz by default. A Raspberry Pi was used to set it to  $f_s = 1$  MHz.

## 5. Part Design

### 5.1. Shielding Boxes

When an alternating current flows through a conductor, the current density is highest near the outside of the conductor and decreases exponentially with depth. This is called the skin effect. The skin depth is the depth at which only  $1/e$  of the current density is left. It depends on the frequency of the current. The skin depth is also the depth at which the amplitude of an electromagnetic wave entering a material is reduced to  $1/e$  of the incident amplitude.

The skin depth of copper is  $65.2 \mu\text{m}$  at 1 MHz, the switching frequency of the converters. A sheet of copper is therefore many times the skin depth in thickness and should be good shielding against the waves radiated by the coils. The simplest method of fabricating a box from copper sheet is cutting out the net of the box and folding the sides up. Three different boxes like this were made by the mechanical workshop of the Institute for Nuclear Physics. Their dimensions, measured on the inside, are shown in Table 5.1. They were chosen so they would fit over the coil of the frontend converter. The edges around the opening of the box were covered in electrical tape to isolate them from the electronics on the board. A photograph of these boxes is shown in Fig. 5.1.

	Box 1	Box 2	Box 3
Length [mm]	22	24	26
Width [mm]	15	15	15
Height [mm]	17	16	17
Wall thickness [mm]	0.5	0.5	0.5

Table 5.1.: Dimensions of the copper boxes used for shielding.

## 5. Part Design



Figure 5.1.: The three copper boxes used as shielding for the frontend board.

## 5.2. Toroidal Coil

### 5.2.1. Plastic Core

A solenoidal coil can simply be wound around a cylindrical object of the required diameter, which is then removed. The production of a toroidal coil is more difficult. To achieve a relatively consistent coil shape, the wire needs to be wound around a core. This core cannot be easily removed from the coil afterwards and therefore needs to be made from a non-ferromagnetic material. The most basic design for such a core is a toroid with a rectangular cross section like the coil itself. To ensure that the windings are equidistant on the outside of the toroid, grooves with the same diameter as the wire were added to the core design. Lastly, a wire cannot be

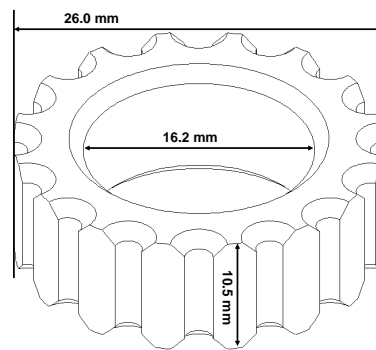


Figure 5.2.: CAD design of the plastic core for the toroidal coil.

bent to an arbitrarily small radius. To make the winding of the coil easier, a chamfer was added to all edges the wire needed to be bent around. A schematic for the core was made using a Computer Assisted Design (CAD) program, which was then fabricated from PVC in the mechanical workshop of the Institute for Nuclear Physics.

## 5. Part Design

### 5.2.2. Optimization of Core Design Parameters

The parameters of the design of the toroid core are its inner radius  $a$ , outer radius  $b$ , height  $h$ , number of windings  $N$  and wire diameter  $w$ . These need to be adjusted, so that several conditions are fulfilled. Firstly, of course, the coil needs the correct inductance for the buck converter. It can be calculated using Equation 3.14. In this equation, the radii and height are measured to the centers of the wires and are therefore given by

$$r_i = a + \frac{w}{2} \quad (5.1)$$

$$r_o = b \quad (5.2)$$

$$H = h + w. \quad (5.3)$$

Furthermore, there needs to be enough space on the inside of the core for the wires to fit. This condition can approximately be expressed as

$$\pi \left( a - \frac{w}{2} \right) \geq Nw. \quad (5.4)$$

This somewhat underestimates the necessary inner radius, as the wires actually touch at a point further in than the circle on which their centers lie. This is not important since adjustments were necessary anyway, as will be discussed later. The DC resistance of the coil can be calculated as

$$R_{DC} = \rho \cdot \frac{l_{\text{wire}}}{\pi \left( \frac{w}{2} \right)^2}, \quad (5.5)$$

where  $\rho$  is the resistivity of the wire material (here:  $\rho_{Cu} = 1.7 \times 10^{-8} \Omega \text{m}$  at room temperature [22]),  $l_{\text{wire}}$  is the length of the wire and  $w$  is the wire diameter. The wire thickness  $w$  needs to be high enough to accommodate the current that will go through it on the board. The toroidal coil is designed for the board powering MuPix and MuTRiG, which have a maximum current of 30 A. For this a thick wire of 2 mm diameter was chosen. One can also reduce  $R_{DC}$  by minimizing the length of wire in the coil, which is approximately

$$l_{\text{wire}} = N \cdot (2H + 2(r_o - r_i)). \quad (5.6)$$

This was not done here, instead the algorithm described below keeps  $N$  as low as possible, which makes for easier construction of the coil. Lastly the outer diameter  $b$  and height  $h$  are constrained by the space available for the coil:

$$2b + w \leq \text{maximum radius} \quad (5.7)$$

$$h + 2w \leq \text{maximum height} \quad (5.8)$$

The values for  $N$  and  $a$  influence each other: A higher  $N$  requires a larger  $a$  to fit the windings. A higher  $a$  on the other hand results in a lower inductance which needs to be compensated for by increasing  $N$ . This was solved using the following algorithm. It is given values for  $L$ ,  $b$ ,  $w$  and the maximum height. It also receives some arbitrary small  $a$ . It then goes through the following steps:

### 5. Part Design

1. With the given  $L$ ,  $r_o = b$  and  $r_i = a + w/2$  find the necessary value of  $N^2H = N^2(h + w)$ .
2. Find the smallest  $N$  for which  $h + 2w$  fits the maximum height.
3. Check if  $a$  is large enough.
4. If  $a$  is too small, adjust it to fit  $N$  windings and repeat from step 1.

This was implemented in a python script and a core was made. When winding it with the wire it turned out that the 2 mm copper wire was much stiffer than anticipated. This caused the wire not to lie snugly around the core. This in turn caused the wires to no longer fit in the inside of the core. After increasing the inner radius the coil could be successfully wound. However, it ended up slightly larger than intended. The finished coil is shown in Fig. 5.3 and its dimensions are listed in Table 5.2.

Outer diameter	32 mm
Inner diameter	7 mm
Total height	16 mm
Inductance at 100 kHz	0.564 $\mu$ H

Table 5.2.: Dimensions and inductance of the toroidal coil. The diameters and height include the wires.



Figure 5.3.: The toroidal air coil used for the measurements.

## 6. Results and Analysis

### 6.1. Efficiency

#### 6.1.1. Effect of Shielding on the Inductance

The inductances measured with the different boxes as shielding are listed in Table 6.1. Compared to the inductance without shielding they are reduced by up to 9.6 %. The fact that the shielding reduces the inductance was expected: The shielding inhibits the magnetic field of the coil, so the voltage that is inducted back into they coil and counteracting the change in the current is reduced, and so in turn is the inductance. It is also to be expected that the inductance is less reduced with a larger box: The larger the box is, the more similar the situation is to their not being any shielding, so the inductance should approach the one without shielding as well. As discussed in section 3.2, the reduced inductance also means a reduced efficiency.

Shielding	Inductance	Reduced by
None	$(6.25 \pm 0.06) \mu\text{H}$	
Box 1	$(5.65 \pm 0.05) \mu\text{H}$	9.6 %
Box 2	$(5.69 \pm 0.05) \mu\text{H}$	9.0 %
Box 3	$(5.70 \pm 0.05) \mu\text{H}$	8.8 %

Table 6.1.: Inductance of a coil for different shielding.

#### 6.1.2. Effect of Shielding on the Efficiency

The efficiency of the frontend board converter with  $V_o = 1.8 \text{ V}$  was plotted against output current in Fig. 6.1, Fig. A.1 and Fig. A.2. The shape of the curve resembles the one expected for a buck converter as seen in Fig. 3.5. The efficiency curves for different shielding are very close to each other and can hardly be distinguished in the plot.

To better compare the efficiencies, the difference in efficiency between measurements with and without shielding were plotted against output current in Fig. 6.2, Fig. A.3 and Fig. A.4. The losses in efficiency are very small, all except one are below 1 %. In some cases even efficiency gains were measured. This contradicts the prediction made in subsection 6.1.1 that the efficiency would go down.

## 6. Results and Analysis

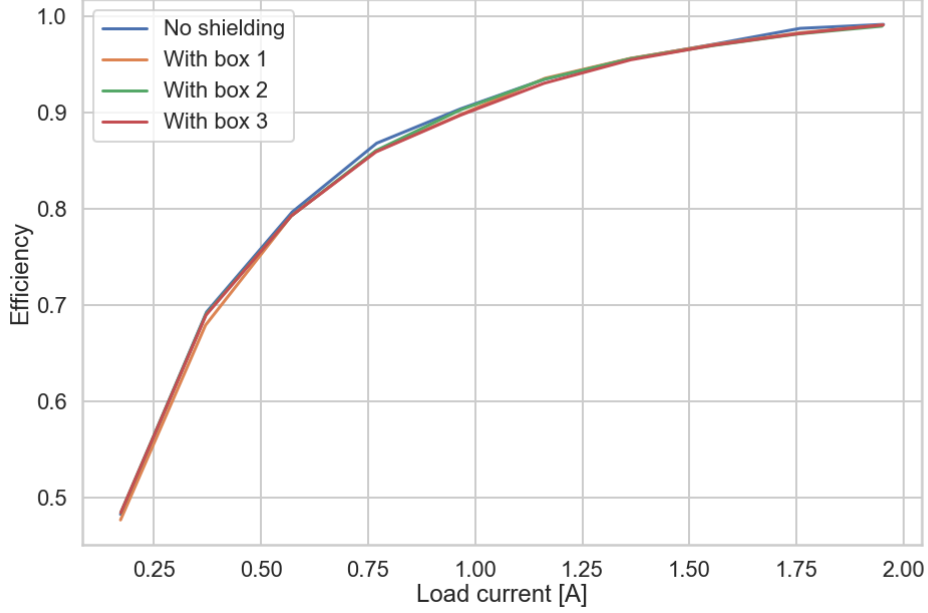


Figure 6.1.: Efficiency of the converter with different shielding at  $V_{in} = 16$  V.

Assuming uncertainties of 0.01 V for  $V_{in}$ , 0.001 A for  $I_{in}$ , 0.01 V for  $V_o$  and 0.6 mV for  $I_o$  based on the lowest digits given by the power supply and the resolution of the analog digital converter used [23], the uncertainty of the efficiency loss can be estimated with gaussian error propagation to be about 0.004. As this is large compared to the differences measured, no good comparison of the different boxes can be made. Also, the gains measured at some load currents are within this uncertainty and likely not real.

It can be concluded from the measurements, that introducing copper boxes as shielding does not cause a significant loss of efficiency. The necessary input power for a given output power and efficiency is

$$P_{in} = \frac{P_o}{\eta}. \quad (6.1)$$

A change  $\Delta\eta$  in efficiency therefore causes an increase in the needed input power of about

$$\Delta P_{in} = -P_o \frac{\Delta\eta}{\eta^2}. \quad (6.2)$$

The frontend board with  $V_o = 1.8$  V is expected to have an output power of 1.8 W at 1 A. With an efficiency of about 0.84 at  $I_o = 1$  A and  $V_{in} = 20$  V a loss in efficiency of  $\Delta\eta = 0.01$  causes an increase in the necessary input power of  $\Delta P_o = 0.0255$  W for a

## 6. Results and Analysis

single converter and 2.86 W for all 112 of these boards, which is very small compared to the total power consumption of the experiment (see Table 2.1).

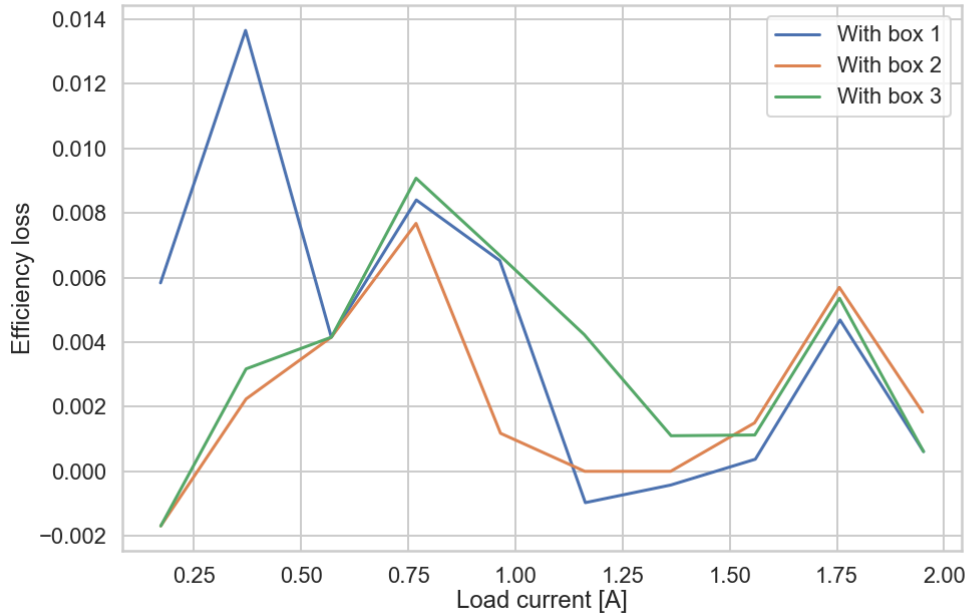


Figure 6.2.: Loss in efficiency of the converter for different shielding at  $V_{in} = 16$  V.

### 6.1.3. Effect of Toroidal Coils on the Efficiency

The efficiency curves of the converter with a solenoidal and toroidal coil were plotted in Fig. 6.3, Fig. A.5 and Fig. A.6. They show the efficiency with the toroid to be consistently higher than the one with the solenoid.

If the coils have the same inductance, then according to Equation 3.11 the efficiency with the toroid should be somewhat worse than the efficiency with the solenoid, as the toroid is wound from a longer wire than the solenoid and therefore has a higher DC resistance. The DC resistance of the toroid was measured to be  $3.0 \Omega$  compared to the  $1.8 \Omega$  of the solenoid. The reason for the difference in efficiency is a mismatch of the inductances. The inductances were measured at 100 kHz to be  $0.564 \mu\text{H}$  for the toroid and  $0.488 \mu\text{H}$  for the solenoid. The benefit of a higher inductance outweighs the higher DC resistance, as it also affects the contribution to the losses of the transistors. Because of the difference in inductance, it is not possible to extract a value for the toroid's effect on the efficiency from this measurement. It can be said, however, that it is small compared to the effect of deviations of the coils' inductances.

## 6. Results and Analysis

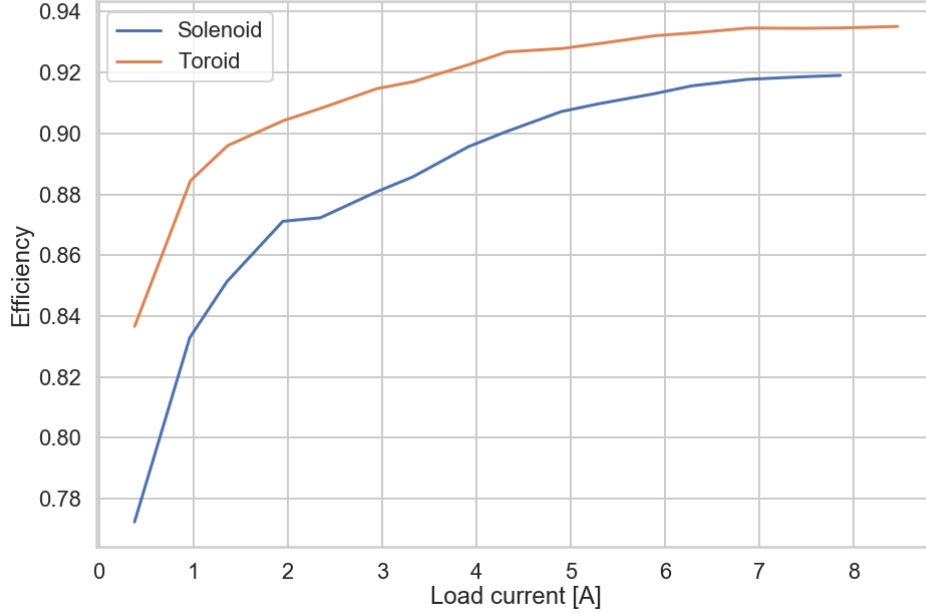


Figure 6.3.: Efficiencies of the converter with solenoidal and toroidal coil at  $V_{in} = 10$ .

## 6.2. Radiated Noise

### 6.2.1. Time Domain Signal

Figure 6.4 shows the voltage at the coil (blue) and the radiated noise picked up by the near field probe (yellow) in the time domain. The voltage at the coil clearly follows the theoretical curve in Fig. 3.4: First it is at  $V_{in} - V_o = 16.2$  V for a short rectangular pulse and then it is at  $-V_o = -1.8$  V for the rest of the period. The frequency of the signal is about 1 MHz, which is the switching frequency of the converter. The duty cycle is about 0.12, which is slightly larger than the 0.1 expected for the conversion from 18 V to 1.8 V. The radiated noise features the same signal, but much weaker and superimposed with several signals. This is expected, as

$$V_{probe} \propto \frac{dB}{dt} \propto \frac{dI_L}{dt} \propto V_L. \quad (6.3)$$

After each flank of the square pulse there is a decaying oscillation with a frequency of about 22.5 MHz. It is unclear whether this is an actual signal in the radiated noise or an effect in the measurement such as reflections of the signal at the oscilloscope.

## 6. Results and Analysis



Figure 6.4.: Time domain signal of the radiated noise and the inductor voltage with  $V_{in} = 18 \text{ V}$  and  $V_o = 1.8 \text{ V}$ .

### 6.2.2. Spectrum of the Frontend Converter

All interesting features of the spectrum of the radiated noise (Fig. 6.5) are at frequencies below 100 MHz. Above this frequency there is only the background, a band with occasional spikes without any recognisable structure. The full spectrum is shown in Fig. A.7.

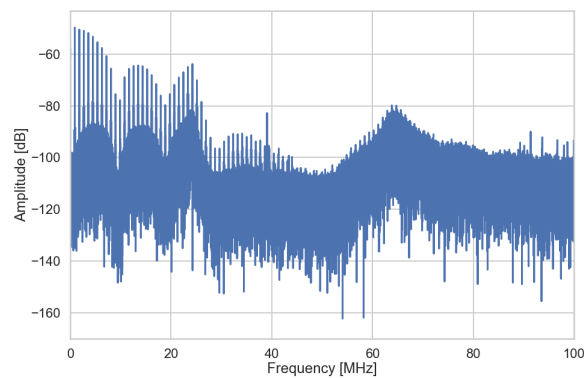


Figure 6.5.: Spectrum of the frontend converter without shielding, measured at position 1.

## 6. Results and Analysis

At the low frequency end the spectrum consists of regular spikes about 0.91 MHz apart. These are the switching frequency and its harmonics. Below these is a structure of bumps, about 10 MHz in width. Some resonance might cause a dip in the signal at 10 MHz and its harmonics, resulting in this structure. Just as with the oscillations observed in the time domain, it is unclear if this is a feature of the converter's radiation or the measurement with the probe. A close up of the first two of these bumps is shown in Fig. 6.6. The last structure in the spectrum is a broad peak around ca. 70 MHz.

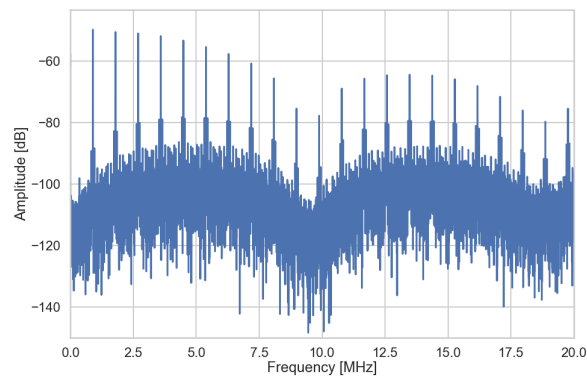


Figure 6.6.: Close up of the spectrum of the frontend converter, measured at position 1.

When the probe is turned by  $90^\circ$ , the spectrum looks mostly the same, except lower in amplitude.

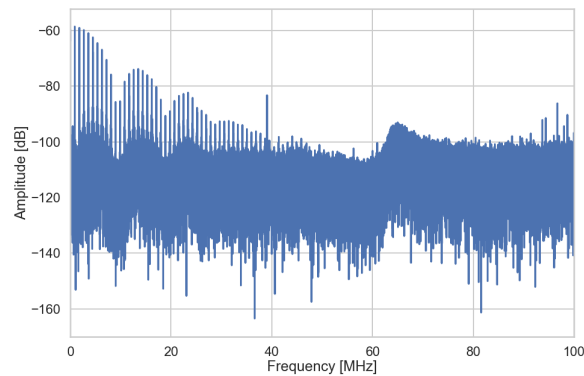


Figure 6.7.: Spectrum of the frontend converter without shielding, measured at position 1 with the probe rotated  $90^\circ$ .

## 6. Results and Analysis

A comparison of the spectra at different distances is shown in Fig. 6.8. With increasing distance from the coil, the amplitude of the signal decreases. At position 3 all structures except the harmonics of the switching frequency have almost entirely vanished in the background.

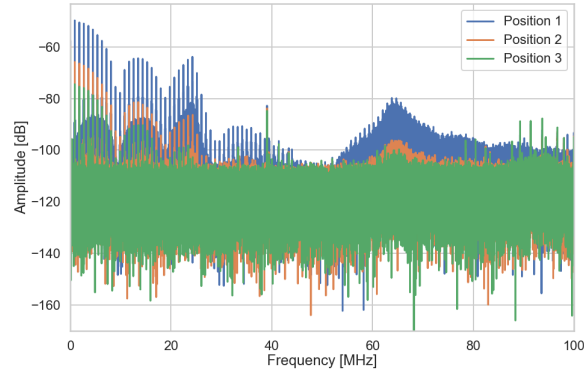


Figure 6.8.: Spectra of the frontend converter without shielding at different distances.

### 6.2.3. Effect of Shielding on the Radiated Noise

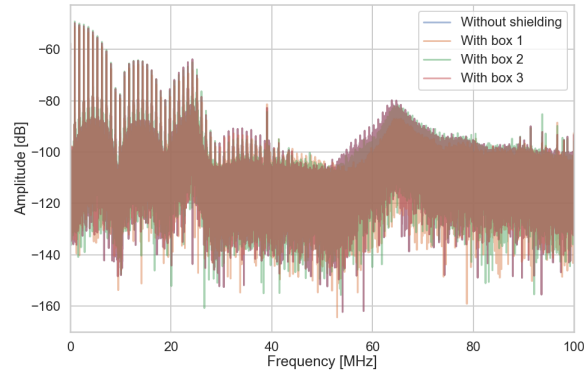


Figure 6.9.: Spectra of the frontend converter with different shielding, measured at position 1.

In Fig. 6.9 the spectra with different shielding as measured at position 1 are plotted for comparison. There is no noticeable difference between the spectra with and without shielding. However, when looking at the signal in the time domain while adding and removing the shielding, there was a visible difference in the height of the rectangular pulse of about 1.56 mV. The signals are shown in Fig. 6.11.

## 6. Results and Analysis

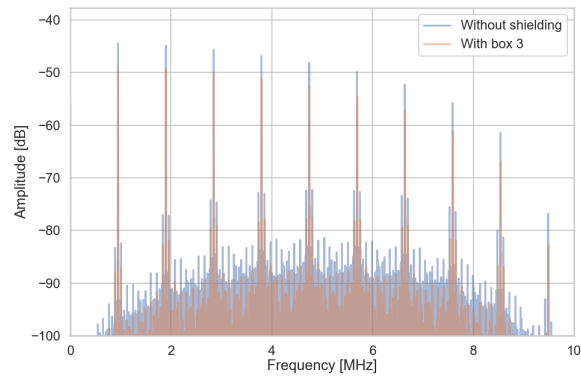


Figure 6.10.: Spectra of the frontend converter with different shielding without changing probe position.

This discrepancy can be explained by the way the frequency domain measurement was conducted: The spectra for a given shielding were taken at all positions, then the shielding was changed. The position and orientation slightly vary after the probe was removed from and reattached to a cable of the noise measurement rig. If the change in amplitude caused by this is large enough, it will obscure the effect of the shielding. To check if this was the case, a new measurement was taken in which the probe remained untouched at position 1 as box three was placed on the coil. The spectra taken this way (Fig. 6.10) show a reduction of the amplitude by up to 5 dB or about 68 % when introducing a copper box as shielding.

## 6. Results and Analysis



(a) Without Shielding.



(b) With box 3.

Figure 6.11.: Time domain signal signal with and without shielding. The cursor positions are the same in both pictures.

## 6. Results and Analysis

### 6.2.4. Effect of Toroidal Coils on the Radiated Noise

The shape of the spectrum with a toroidal coil for the most part resembles the one with a solenoidal coil. The exception is a broad bump in the spectrum with the toroid at about 300 MHz. At low frequencies the amplitude of the spectrum with the toroid is much reduced compared to the spectrum with the solenoid. A closer view of this frequency range (Fig. 6.13) shows a reduction of up to 30 dB, which is equivalent to a factor of 1000.

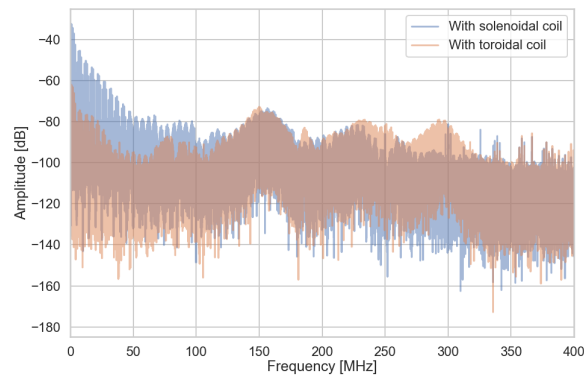


Figure 6.12.: Comparison of the spectra with solenoidal and toroidal coil.

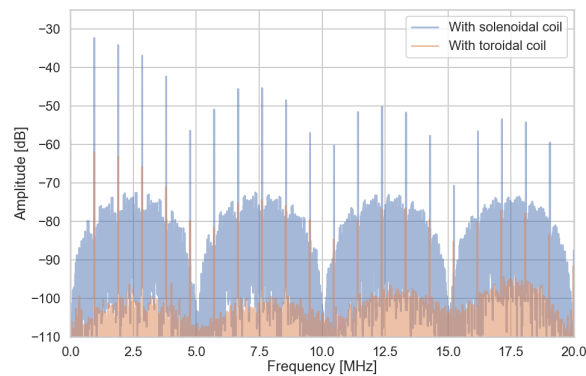


Figure 6.13.: Close up of the spectra with solenoidal and toroidal coil.

## 6. Results and Analysis

### 6.2.5. Noise Radiated by the Wires

At a frequency of about 150 MHz a broad bump is present, with about the same amplitude in both spectra. It is still visible at the largest distance from the coil with the probe rotated by  $90^\circ$  (see Fig. 6.14), even though the peaks of the switching frequency and its harmonics are much reduced in this position. This indicates that it is not part of the radiation of the coil at all.

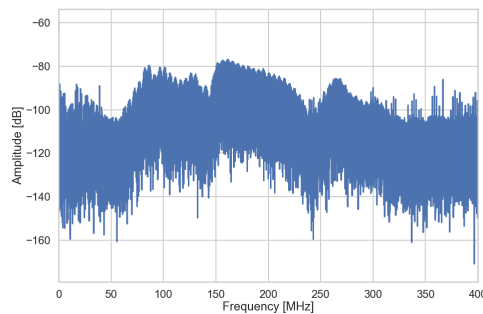


Figure 6.14.: Spectrum of the noise radiated by a solenoid, measured at position 3 with the probe rotated  $90^\circ$ .

In the noise measurement setup, the probe was close to the wires for the input voltage. Any alternating current in these causes a changing magnetic field around them, which was then picked up by the probe. To confirm this, another spectrum (Fig. 6.15) was taken, with the probe held next to the wires but as far away as possible from the converter.

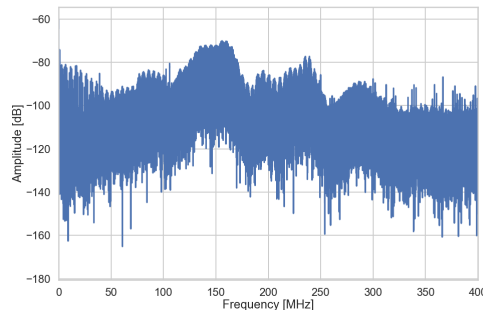


Figure 6.15.: Spectrum of the noise radiated by the wires.

## *6. Results and Analysis*

The bump is still visible in this spectrum, in fact its amplitude is increased as the probe was held as close as possible to the wires on purpose. While the noise radiated by the wires is not as strong as the one radiated by the coils, it indicates the presence of conducted noise in the wires, which needs to be controlled so it does not disturb the electronics up- and downstream. This might be achieved by adding additional low pass filters to the converters.

## 7. Conclusion and Outlook

The Mu3e experiment requires a powering scheme capable of functioning in the experiment's 1 T magnetic field. This will be achieved using DC-DC buck converters with air coils. These radiate electromagnetic waves, which need to be reduced to ensure proper functioning of the various electronics in the experiment.

In this thesis two methods of reducing the radiation were investigated: Covering the coils with a shielding and replacing solenoidal coils with toroidal ones. Copper boxes and a toroidal coil were designed to fit the spatial restrictions in the experiment and then tested for their effectiveness.

The measurements that were done show that both these methods are viable for reducing the electromagnetic noise radiated by buck converters. The shielding provides a reduction of about 5 dB compared to the unshielded coil. The toroidal coil radiates about 30 dB less than a solenoid. Efficiency measurements show that neither shielding nor toroidal coils cause significant losses in efficiency. Their benefits should therefore outweigh their drawbacks.

While the copper boxes used in the test did provide a measurable shielding, they performed worse than expected. The shielding needs to be further investigated, possible improvements include:

- Using thicker material for the shielding
- Completely enclosing the coil
- Shielding the entire converter instead of just the coil
- Using a different method for producing the shielding, such as milling it out of a block of copper

While the design of the toroidal coil performed well, it could still be tweaked, for example to minimize the DC resistance of the coil. Similar optimizations have previously been performed for buck converters for the CMS experiment [13]. There is also the issue of production: A practical way to make 112 of these coils needs to be found for the assembly of Mu3e.

For future tests, the noise measurement setup could be refined by using professionally made probes, an xy-table and a spectrum analyzer instead of the oscilloscope.

## *7. Conclusion and Outlook*

During the tests it was noticed that the efficiency of a converter strongly depends on the inductance of the coil used. There might, however, be a trade off between the efficiency gained by increasing the inductance and an increase in radiation. Also observed was conducted noise in the input and output wires, which needs to be reduced by way of additional filters.

## Bibliography

- [1] Bogdan Povh, Klaus Rith, Christoph Scholz, Frank Zetsche, and Werner Rodejohann.  
“The Lepton Families”.  
In:  
*Particles and Nuclei: An Introduction to the Physical Concepts*.  
Berlin, Heidelberg: Springer Berlin Heidelberg, 2015,  
Pp. 141–142.  
ISBN: 978-3-662-46321-5.  
DOI: 10.1007/978-3-662-46321-5\_10.  
URL: [https://doi.org/10.1007/978-3-662-46321-5\\_10](https://doi.org/10.1007/978-3-662-46321-5_10).
- [2] Bogdan Povh, Klaus Rith, Christoph Scholz, Frank Zetsche, and Werner Rodejohann.  
“Lepton Number Conservation”.  
In:  
*Particles and Nuclei: An Introduction to the Physical Concepts*.  
Berlin, Heidelberg: Springer Berlin Heidelberg, 2015,  
Pp. 142–143.  
ISBN: 978-3-662-46321-5.  
DOI: 10.1007/978-3-662-46321-5\_10.  
URL: [https://doi.org/10.1007/978-3-662-46321-5\\_10](https://doi.org/10.1007/978-3-662-46321-5_10).
- [3] Ann-Kathrin Perrevoort.  
“The Rare and Forbidden: Testing Physics Beyond the Standard Model with Mu3e”.  
In: *arXiv e-prints*, arXiv:1812.00741 (Dec. 2018), arXiv:1812.00741.  
arXiv: 1812.00741 [hep-ex].
- [4] Niklaus Berger.  
“The Mu3e Experiment”.  
In: *Nuclear Physics B - Proceedings Supplements* 248-250 (2014). 1st Conference on Charged Lepton Flavor Violation, pp. 35–40.  
ISSN: 0920-5632.  
DOI: <https://doi.org/10.1016/j.nuclphysbps.2014.02.007>.  
URL: <http://www.sciencedirect.com/science/article/pii/S0920563214000085>.
- [5] Ivan Perić.  
“A novel monolithic pixelated particle detector implemented in high-voltage CMOS technology”.

## Bibliography

- In: *Nuclear Instruments and Methods in Physics Research Section A: Accelerators, Spectrometers, Detectors and Associated Equipment* 582.3 (2007), pp. 876–885.
- [6] Ann-Kathrin Perrevoort.  
“Searching for Lepton Flavour Violation with the Mu3e Experiment”.  
In: *arXiv e-prints*, arXiv:1802.09851 (Feb. 2018), arXiv:1802.09851.  
arXiv: 1802.09851 [physics.ins-det].
- [7] H. Chen, K. Briggli, P. Eckert, T. Harion, Y. Munwes, W. Shen, V. Stankova, and H.C. Schultz-Coulon.  
“MuTRiG: a mixed signal Silicon Photomultiplier readout ASIC with high timing resolution and gigabit data link”.  
In: *Journal of Instrumentation* 12.01 (Jan. 2017), pp. C01043–C01043.  
DOI: 10.1088/1748-0221/12/01/c01043.  
URL: <https://doi.org/10.1088/1748-0221/12/01/c01043>.
- [8] Dorothea vom Bruch.  
“Online Data Reduction using Track and Vertex Reconstruction on GPUs for the Mu3e Experiment”.  
In: *European Physical Journal Web of Conferences*.  
Vol. 150.  
Aug. 2017,  
P. 00013.  
DOI: 10.1051/epjconf/201715000013.
- [9] Cristian Alejandro Fuentes Rojas.  
“Optimization of the design of DC-DC converters for improving the electromagnetic compatibility with the Front-End electronic for the super Large Hadron Collider Trackers”.  
Presented 25 Nov 2011.  
2011.  
URL: <https://cds.cern.ch/record/1416785>.
- [10] *Efficiency of Buck Converter*.  
URL: [http://rohmfs.rohm.com/en/products/databook/applinote/ic/power/switching\\_regulator/buck\\_converter\\_efficiency\\_app-e.pdf](http://rohmfs.rohm.com/en/products/databook/applinote/ic/power/switching_regulator/buck_converter_efficiency_app-e.pdf).  
Application note by ROHM Semiconductor (accessed 01.07.19).
- [11] *Using the TPS53819AEVM-123 Wide Input Voltage, Eco-mode, Single Synchronous Step-Down Controller with PMBus*.  
URL: <http://www.ti.com/lit/ug/slvu719a/slvu719a.pdf>.  
(accessed 08.07.19).
- [12] Hantaro Nagaoka.  
“The inductance coefficients of solenoids”.  
In: *Journal of the College of Science* 27.3 (1909), p. 31.
- [13] L Feld, R Jussen, W Karpinski, K Klein, J Sammet, and M Wlochall.

## Bibliography

- “Radiated electromagnetic emissions of DC-DC converters”.  
In: *Journal of Instrumentation* 5.12 (Dec. 2010), pp. C12055–C12055.  
DOI: 10.1088/1748-0221/5/12/c12055.  
URL: <https://doi.org/10.1088/1748-0221/5/12/c12055>.
- [14] *Inductance of a Toroid*.  
URL: <http://www.phys.uri.edu/gerhard/PHY204/ts1267.pdf>.  
(accessed 08.07.19).
- [15] Ronald Decker.  
*A Simple Method to Measure Unknown Inductors*.  
URL: <https://www.dos4ever.com/inductor/inductor.html>.  
(accessed 02.07.19).
- [16] *Capacitance and Inductance Measurements Using an Oscilloscope and a Function Generator*.  
URL: <https://de.tek.com/document/application-note/capacitance-and-inductance-measurements-using-oscilloscope-and-function-generator>.  
Application note by Tektronix (accessed 02.07.17).
- [17] *BK Precision Model 880 Dual Display LCR Meter Instruction Manual*.  
URL: [https://bkpmedia.s3.amazonaws.com/downloads/manuals/en-us/880\\_manual.pdf](https://bkpmedia.s3.amazonaws.com/downloads/manuals/en-us/880_manual.pdf).  
(accessed 02.07.19).
- [18] *Tenma 72-2635 Manual*.  
URL: <https://www.lion.co.il/d?id=F53BWN&pos=5>.  
(accessed 02.07.19).
- [19] Douglas C. Smith.  
*An Easy to Build Shielded Magnetic Loop Probe*.  
URL: <https://www.emcesd.com/tt120100.htm>.  
(accessed 03.07.19).
- [20] *Beehive Electronics 100 Series EMC Probes*.  
URL: <https://www.meilhaus.org/downloadserver/bee hive/bee hive-100.pdf>.  
(accessed 03.07.19).
- [21] *Tektronix DPO 5000B Series User Manual*.  
URL: <https://www.tek.com/oscilloscope/dpo70000-mso70000-manual/mso70000dx-dpo70000dx-mso70000c-dpo70000c-dpo7000c-mso5000b-0>.  
(accessed 04.07.19).
- [22] R. A. Matula.  
“Electrical resistivity of copper, gold, palladium, and silver”.  
In: *Journal of Physical and Chemical Reference Data* 8.4 (1979), pp. 1147–1298.  
DOI: 10.1063/1.555614.  
eprint: <https://doi.org/10.1063/1.555614>.  
URL: <https://doi.org/10.1063/1.555614>.

## *Bibliography*

- [23] *LabJack U3 Data Sheet*.  
URL: <https://labjack.com/support/datasheets/u3/appendix-a>.  
(accessed 12.07.19).

## List of Tables

2.1. Voltage and power requirements for ASICs and on-detector electronic components inside of the magnet. . . . .	8
5.1. Dimensions of the copper boxes used for shielding. . . . .	22
5.2. Dimensions and inductance of the toroidal coil. The diameters and height include the wires. . . . .	25
6.1. Inductance of a coil for different shielding. . . . .	26
A.1. Parameters for the noise measurements. . . . .	47

## List of Figures

2.1.	Feynman graphs for possible channels for the $\mu \rightarrow eee$ decay. . . . .	3
2.2.	Feynman graph of the internal conversion process. . . . .	4
2.3.	Topology of a $\mu \rightarrow eee$ event and an example of combinatorial background. . . . .	5
2.4.	Schematic of the different detectors in the Mu3e experiment. An example of tracks from a $\mu \rightarrow eee$ event is shown, with the positrons in red and the electron in blue. . . . .	5
2.5.	Sketch of a high voltage monolithic active pixel sensor (from [5]). . . . .	6
2.6.	Readout scheme of the Mu3e experiment. The yellow area indicates the electronics which are inside of the magnet (from [8]). . . . .	7
3.1.	Schematic of a simple DC-DC buck converter (adapted from [9]). . . . .	9
3.2.	The voltage at the switching node (adapted from [9]). . . . .	9
3.3.	The two stages of the operation of a buck converter. The red lines indicate the current (from [9]). . . . .	10
3.4.	Inductor voltage and current over time (from [9]). . . . .	11
3.5.	Efficiency curve of the TPS53819A buck converter (from [11]). . . . .	12
3.6.	A toroidal coil with rectangular cross section (adapted from [14]). . . . .	13
4.1.	Setup for measuring an inductor (green box) via the impedance (from [16]). . . . .	14
4.2.	Example measurement of an inductor at the different frequencies of the LCR meter. . . . .	16
4.3.	Efficiency measurement setup. a) power supply b) load generator c) LabJack connecting load generator to computer d) Raspberry Pi e) MuPix converter. . . . .	17
4.4.	The noise measurement setup. a) power supply b) load generator c) oscilloscope d) front end converter e) noise measurement rig with probe. . . . .	17
4.5.	Schematic of the magnetic near field probe (adapted from [19]). . . . .	18
4.6.	The magnetic near field probe used for the noise measurements. . . . .	18
4.7.	Output power at 1 mT of different loop probes against frequency (from [20]). . . . .	19
4.8.	The noise measurement rig with the four probe positions. . . . .	19
5.1.	The three copper boxes used as shielding for the frontend board. . . . .	23
5.2.	CAD design of the plastic core for the toroidal coil. . . . .	23
5.3.	The toroidal air coil used for the measurements. . . . .	25
6.1.	Efficiency of the converter with different shielding at $V_{in} = 16$ V. . . . .	27

*List of Figures*

6.2. Loss in efficiency of the converter for different shielding at $V_{in} = 16$ V. . . . .	28
6.3. Efficiencies of the converter with solenoidal and toroidal coil at $V_{in} = 10$ . . . . .	29
6.4. Time domain signal of the radiated noise and the inductor voltage with $V_{in} = 18$ V and $V_o = 1.8$ V. . . . .	30
6.5. Spectrum of the frontend converter without shielding, measured at position 1. . . . .	30
6.6. Close up of the spectrum of the frontend converter, measured at position 1. . . . .	31
6.7. Spectrum of the frontend converter without shielding, measured at position 1 with the probe rotated $90^\circ$ . . . . .	31
6.8. Spectra of the frontend converter without shielding at different distances. . . . .	32
6.9. Spectra of the frontend converter with different shielding, measured at position 1. . . . .	32
6.10. Spectra of the frontend converter with different shielding without changing probe position. . . . .	33
6.11. Time domain signal signal with and without shielding. The cursor positions are the same in both pictures. . . . .	34
6.12. Comparison of the spectra with solenoidal and toroidal coil. . . . .	35
6.13. Close up of the spectra with solenoidal and toroidal coil. . . . .	35
6.14. Spectrum of the noise radiated by a solenoid, measured at position 3 with the probe rotated $90^\circ$ . . . . .	36
6.15. Spectrum of the noise radiated by the wires. . . . .	36
A.1. Efficiency of the converter with different shielding at $V_{in} = 18$ V. . . . .	47
A.2. Efficiency of the converter with different shielding at $V_{in} = 20$ V. . . . .	48
A.3. Loss in efficiency of the converter for different shielding at $V_{in} = 18$ V. . . . .	48
A.4. Loss in efficiency of the converter for different shielding at $V_{in} = 20$ V. . . . .	49
A.5. Efficiencies of the converter with solenoid and toroid coil at $V_{in} = 12$ . . . . .	49
A.6. Efficiencies of the converter with solenoid and toroid coil at $V_{in} = 14$ . . . . .	50
A.7. Full spectrum of the noise radiated by the front end converter without shielding, measured at position 1. . . . .	50

## A. Appendix

	Converter for MuPix	Converter for frontend board
$V_{in}$	12 V	20 V
$V_o$	2.2 V	1.9 V
$I_o$	8.0 A	1 V
$f_s$	1 MHz	1 MHz
Sample rate	2.5 GS/s	2.5 GS/s
Vertical scale	7 mV/div	7 mV/div
Horizontal scale	100 $\mu$ s/div	100 $\mu$ s/div

Table A.1.: Parameters for the noise measurements.

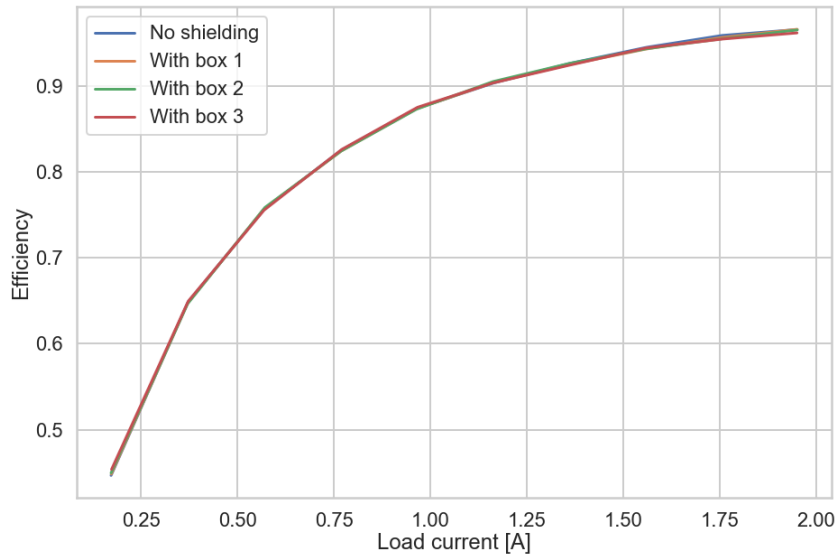


Figure A.1.: Efficiency of the converter with different shielding at  $V_{in} = 18$  V.

A. Appendix

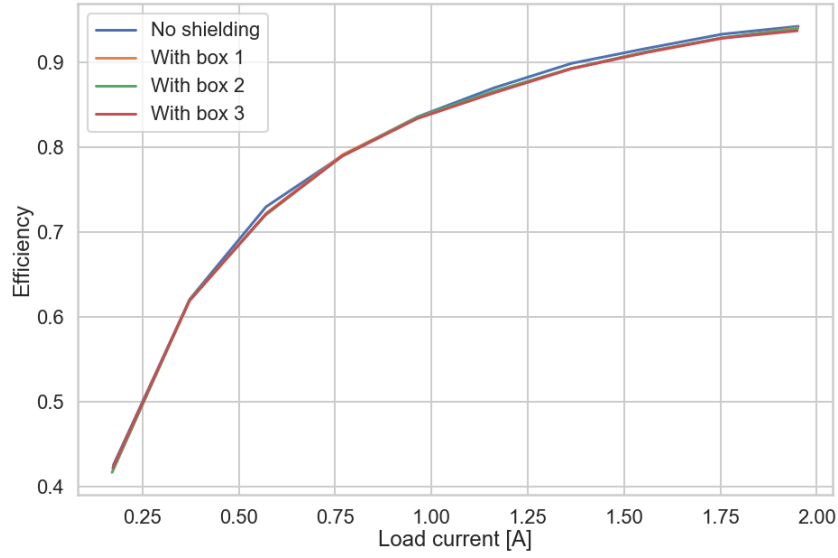


Figure A.2.: Efficiency of the converter with different shielding at  $V_{in} = 20$  V.

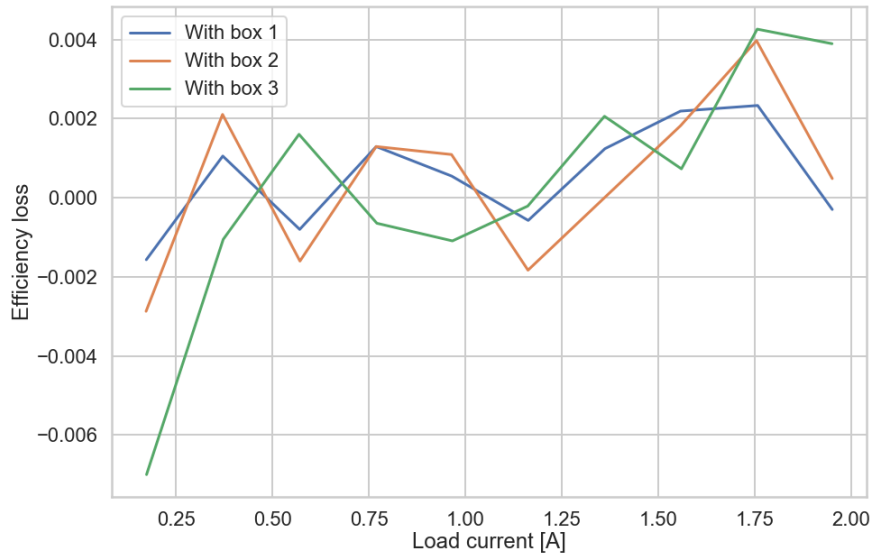


Figure A.3.: Loss in efficiency of the converter for different shielding at  $V_{in} = 18$  V.

A. Appendix

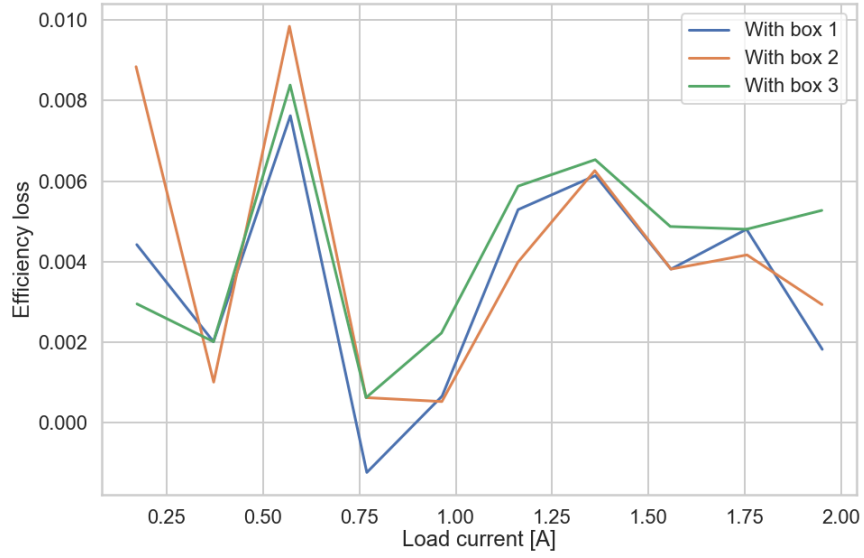


Figure A.4.: Loss in efficiency of the converter for different shielding at  $V_{in} = 20$  V.

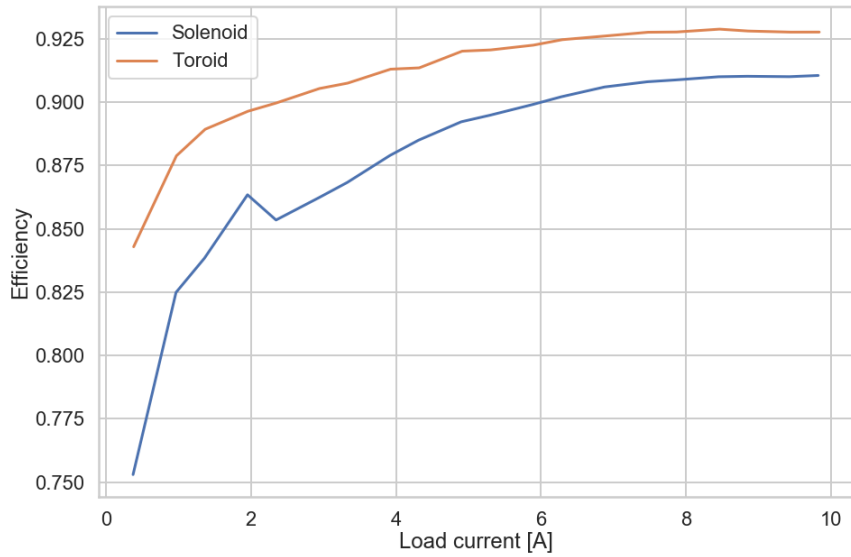


Figure A.5.: Efficiencies of the converter with solenoid and toroid coil at  $V_{in} = 12$ .

A. Appendix

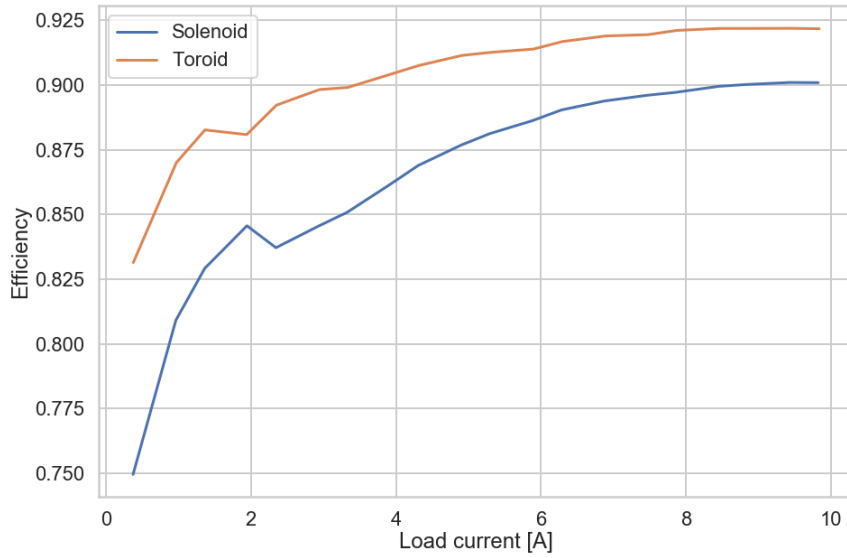


Figure A.6.: Efficiencies of the converter with solenoid and toroid coil at  $V_{in} = 14$ .

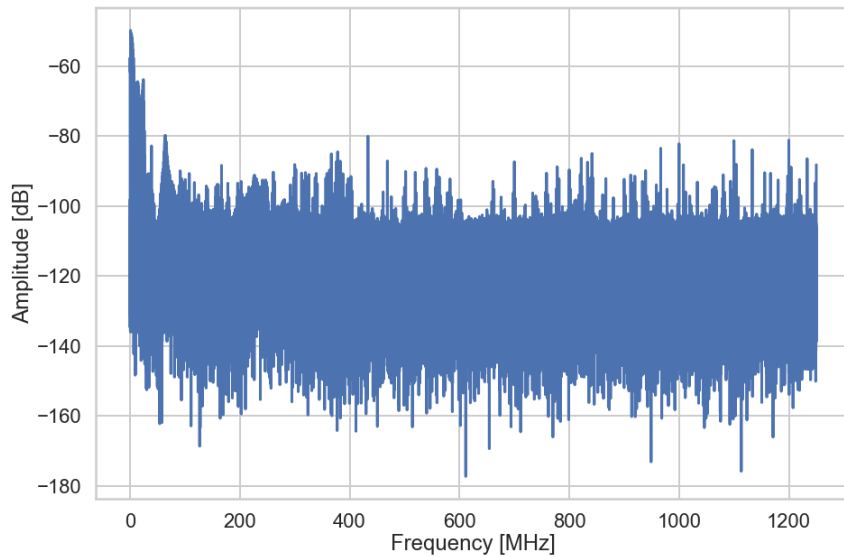


Figure A.7.: Full spectrum of the noise radiated by the front end converter without shielding, measured at position 1.